

Response to referee #1's comments

The authors would like to thank the referee for his/her input. We appreciate very much the time they took. Please find below a point to point reply to the comments. Below we provide a point by point response and state the changes made to the manuscript. Changes made in the manuscript are marked in yellow.

The comments were very helpful. Some of them pointed corrections that needed to be made to the data analysis, in particular the inversion result and its discussion. Thanks to the constructive comments the manuscript has significantly improved. At this point a revised manuscript is not mandatory. However, a revision with preliminary figures and changes marked has been uploaded to facilitate the editorial decision.

As a result to the comments we have produced a revised manuscript that has improved significantly in the substantial concerns raised by the reviewer, which were

- An error estimate of the inversion has been included
- Inconsistencies between synthetic and real data inversion have been analyzed and are discussed, the reason why the resolution achievable was low has been assessed and is discussed in the revised manuscript
- More details on the inversion procedure are given, making it easier to follow the methods used

We also attempted to make the “take home message” clearer: Despite data unfavorable for inversion (as acquired one-sided), we obtain a good result that is consistent with independent measurements, it may even be useful for situations where one-sided acquisition is required. Future experiments will evaluate this. In fact, after all the assessment and more inversion tests the inverted CO₂ concentration map is qualitatively the same, the magnitude of the values has changed. This fortifies our confidence about the result.

General Comment:

The manuscript describes tomographic determination of the 2D distribution of the CO₂ mixing ratio (XCO₂) derived from a series of line integrated CO₂ measurements (or CO₂ column density measurements). While the overall structure of the paper is straightforward, there are many unclear points, missing information, and not very convincing statement, which make the paper rather hard to read and understand (see detailed list below). In particular the tomographic inversion is not convincing at all. It remains unclear why only such a small spatial resolution is reached. Also, no attempt is made to quantify the errors of the tomographic inversion and there are ample indications in the manuscript that they are huge. In summary, the manuscript describes an interesting approach, but the analysis of the data is poor and the errors of the derived fluxes are essentially unknown. I can not recommend publication of the manuscript in its present form.

Clearly, the manuscript needs further work and the points you raised are a helpful guideline. I agree with many of them. However, it strikes me that the inversion result is not convincing, simply because it converged to a result that obviously agrees with previous work (see discussion and references given in the manuscript), both in terms of the distribution of the CO₂ and the computed flux! This has to be made clearer in the manuscript. Details are given in the point to point replies.

1) Page 1, line 17 (abstract): What are 1-D profiles?

A 1-D profile is a graph showing column integrated CO₂ path length concentration product (hereafter called CO₂ path-amounts) versus lateral position (such as scanning angle). In the manuscript, we added column integrated 1-D profiles in the abstract and added an explanation in the introduction in line 28.

2) Page 1, lines 18-19 (abstract): What is the meaning of the phrase "Acquisition was performed from a single half space only" ?

A half space is one of the two parts the Euclidian space is divided into by a plane, meaning the feature was measured from one side only and not from opposite sides. "The acquisition was performed from a single half space only" changed to ". The scan was performed one-sided ". Also at p10, l11 "one-sided" has been added.

3) Page 1, lines 21-22 (abstract): "The method has important implications .." This is not treated in the text, other than saying that retrievals of this kind are difficult.

The implications are for general measurements of that kind (one-sided), such as perhaps airborne scans using that instrument. The conclusions touch on that. To make it clearer "which indicates this tomography method to be **potentially** beneficial for scanning strongly non-isotropic CO₂ distributions, such as diffuse emissions, that can be viewed from limited angles only, **sites difficult to access (e.g. volcanic craters), or airborne acquisitions.**" has been amended on p11, l31.

4) Page 2, lines 21-22: Why can "hard target DIAL" systems use continuous lasers and why is this an advantage?

There are also pulsed hard target DIAL systems, but, due to the lasers, they are much larger and heavier, while cw lasers can be very compact (e.g. fiber lasers) but due to their low peak power (if modulated or pulsed) they need a topographic target (hard target). The point here was to say that we do not measure range resolved CO₂ concentrations and hence no 2D maps. To improve that, at p2, l22 we changed the phrase to "active remote sensing platforms based on hard target DIAL (topographic target DIAL) using continuous wave lasers can be made compact, rugged and portable, which is desirable for platform independent measurement of atmospheric CO₂, be it ground based or air-borne (Sakaizawa et al., 2013; QueiBer et al., 2015a)." and p2, l27 "Hence, during a scanning measurement, no 2D concentration maps are obtained, but 1-D profiles of path amounts, that is, values of path amounts versus scanning angle.

5) Page 2, line 25: The term concentration (i.e. number density or mass/unit volume) is used as synonymous with mixing ratio (e.g. given in ppm)

You are right. But in the Earth science community one seems to often confuse concentration with mixing ratio. I was even asked to change mixing ratio to concentration in another paper! At that point in the manuscript concentration or mixing ratio is not really relevant, but it is as of section 2.2. Consequently, we now use the correct term mixing ratio wherever we talk about [ppm].

6) Page 2, lines 34-35 (last Sentence): This statement is incorrect. Flux (through a particular plane) is obtained by integrating over the CO₂ concentration-distribution weighted by wind speed component perpendicular to the plane.

You are absolutely right. This phrase is misleading and does not contain new information so we have deleted it.

7) Page 3, lines 20, 25: Explanation of delta tau from line 25 should occur after line 19.
Has been moved to after line 19.

8) Page 3, line 30: The position of the glass wedge and the integrating sphere are not clear from Fig. 2, in fact it appears that the emitted beam passes through the sphere. It should be mentioned that the reference detector measures $P(\lambda_{ON})_{ref}$ and $P(\lambda_{OFF})_{ref}$, respectively.

Fig. 2 is just schematically depicting the instrument and lacks the actual instrument details. You have correctly noticed that the emitted beam passes through the sphere. The beam pick is a glass wedge. This has been added to the figure caption for more clarity: "The beam pick is a glass wedge and reflects part of the transmitted light back into an integrating sphere (depicted as diffuser)." We have added on p4, l2: A glass wedge scatters a fraction of the transmitted light into an integrating sphere where the reference detector is mounted, which measures $P(\lambda_{ON})$ and $P(\lambda_{OFF})$ and also added that light of both wavelengths is transmitted simultaneously, which should make it clear.

9) Page 4, lines 1-5: A lot more information needs to be given: What is the divergence of the emitted beam? What is the field of view of the receiving telescope? These quantities are required (a) to calculate the returned power (the quoted "few nW" can only be reached (at R=1 km) when the aperture angles of transmitting and receiving optics exactly match, is this the case? (b) The same quantities are needed to calculate delta Speckle in Eq. (5).

We have added these parameters at page 4. As a matter of fact, the received signal voltage corresponds to a few nW optical power after optimizing the overlap between beam spot on target and telescope field of view. The divergence was 1.7 mrad while the FOV was 1.5 mrad. That means we are wasting some power but that had the purpose to minimize hard target speckle noise. Also, it makes alignment easier. We have added a reference to Queisser et al, 2016 where these details can be found as well as the measurement procedure.

10) Page 4, line 9: What was the delta sigma used to convert delta tau to CO₂ concentrations and mixing ratios)?

Delta sigma was not computed as we used a calibration delta tau (ppm.m) = $X_{CO_2} \times R$ to retrieve CO₂ path amounts (ppm.m) measured just before the scans. The use of ppm.m is common for FTIR absorption spectroscopy and has been adopted here. "However, to retrieve CO₂ path amounts the left hand side of Eq. (1) was not used." added in p4 l13. Reference to Queißer et al. 2016 is given again in manuscript.

11) Page 4, line 9: What could be the reason of the "instrumental offset"? Could it be an effect of differential reflectivity (different reflectivity for lambda on and lambda off) of the target? If this was the case then for each target (i.e. each measurement direction in a scan) there would be a different offset. Was this possibility checked?

We know quite well what the reason is. It's because in reality in Eq. 1, right hand side there is an instrumental tau (λ_{ON}) and a tau (λ_{OFF}). This wavelength dependent optical depth adds a nonstationary offset. It is related for instance to etalon effects at optical interfaces in the instrument. This is well known (for instance, Abshire et al., 2010, Tellus 62B, 770-783, 2010 or Kameyama et al., Appl. Optics, 50, 2010 and a major issue for DIAL. It took us 2 years of work to identify that and get this under control. Different reflectivity for lambda on and lambda off is unlikely as we multiplex and simultaneously transmit λ_{ON} and λ_{OFF} . Then there is an offset caused by hard target speckle, which was accounted for in the measurement precision (which is actually quite low). Speckle noise was not the dominant noise, but the drift of the nonstationary offset. Again, this is why the precision was relatively low, but this did not impede us from going out

there and measure CO₂. The flux is huge so we still got nice results. We have now iterated the instrument further and reached a higher precisions to sense more subtle emissions.

12) Page 4, line 12: Why were mixing ratios calculated? For the flux determination (Eq. 8) the mixing ratios are re-converted to concentrations. While concentrations - as determined from the optical density - are independent of temperature and pressure, mixing ratios are not, so which temperature and pressure was assumed to calculate the values given in Figures 3ff?

As mentioned in 10, we used a calibration, which was based on an in situ measurement which yielded XCO₂ in ppm. This was multiplied by the distance. A number of delta tau was obtained, hence our calibration curve. This is a pertinent question, mixing ratios depend on temperature and pressure. This is not the best method, for the reasons you mention, but it is a pragmatic and viable method that works. The calibration was performed at quasi the same time as the in-plume measurement. For computing number density we used temperature, pressure and relative humidity from a meteorological station placed next to the instrument during the measurement. Since the meteorological parameters varied during the course of a few hours (time of measurements), temperature and humidity slightly changes, so there are errors, but they are small compared to the instrument's error and were therefore not considered. Typically, variations were of the order of 4°C for air T (from 11 to 15 °C), and 10% for RH (between 55% and 65%). The air pressure was steady around 974 hPa. So Nair (at 11 °C, 65% RH, 974 hPa) = 2.47049E25 m⁻³, and Nair (at 15 °C, 55%, 970 hPa) = 2.43487E25 m⁻³, leading to a bias of 1.5%, which, in a simplified estimation, would correspond to typically around 9 ppm of total column averaged mixing ratio. To put this into context, the error of the column averaged mixing ratio is typically ~110 ppm, the error of the in-plume XCO₂ 187 ppm. The resulting flux error would increase by ~0.3 %. Again, I agree that, although given the rather less precise measurement the error arising from the usage of ppm.m instead of m⁻³ or m⁻² is small but it needs to be discussed in the manuscript as it is clearly a crutch and not the optimum . A paragraph has been added in the discussion, p9 111.

13) Page 4, line 17: What were typical values of the three contributions to the error of the right-hand side of Eq. (3)?

Typically, the relative error amounts to 5% of the total path amount ($\sqrt{20^2 + (1\text{m}/150\text{m})^2 + (3\text{e-}3)^2}$), or in absolute terms ~1E23 molecules.m⁻² of CO₂.

14) Page 4, line 19: What were typical values of the SNR?

Typically, sigma GR was around 1/8E-3 with associated SNR of roughly 20.

15) Page 4, lines 26-28: What are typical values of D, Xie, and the resulting delta Speckle (see comment 9, above).

Relative errors related to speckle were between 1 and 3 per thousand (or 0.1-0.3 %) (D=25 cm, Xie = 42 cm).

16) Page 5, line 3: What is the meaning of the term "absolute Cartesian coordinates?" in this context?

Columns of heading angle and corresponding path length were associated with Cartesian coordinates (to work with Matlab which is based on matrices). The term absolute is confusing and has been removed. We added: To be able to apply Eq. (7) to the measured Y_{CO₂}, the associated paths and their angles (hereafter also referred to as rays) were mapped onto (x,y) coordinates using $x_{j,k} = r_{j,k} \cos \Delta\varphi_j$ and $y_{j,k} = r_{j,k} \sin \Delta\varphi_j$. φ_j is the cumulative heading angle of the jth ray

determined from the scanning angular velocity and the time interval between the rays retrieved from the time stamps of the data. For a given ray, $r_{j,k}$ is the k^{th} path length increment, such that $\sum_{k=1}^N r_k = R_j$. N is chosen such that adjacent x_j and y_j were no more than ~ 1 m apart. Since the $\Delta\varphi_i$ are only relative to the first ray the $x_{j,k}$ and $y_{j,k}$ were rotated to match the world coordinate system (i.e. rotated such that the first ray's (x,y) coordinates match the real ray trajectory). This was performed using the well know rotation matrix with a rotation angle, which is the angle between the first ray and the x-axis. The Y_{CO_2} versus the resulting (x,y) coordinates formed the inversion input file (see Table 1 for an example). From the data in that input file an algorithm built the geometry matrix L by associating the (x,y) coordinates with the n model grid cells. Part of the input data file is shown to illustrate the process in Table 1 (now added). Also changed was “where L is a $m \times n$ matrix, called geometry matrix, containing the length of all m rays for all n grid cells” and “ is a $m \times 1$ matrix containing the measured (observed) Y_{CO_2} for each ray, retrieved from the inversion input file”. We hope this paragraph is clearer now.

17) Page 5, line 8: Do the authors here not just mean that the assumed CO₂ concentration within a grid cell is constant (which would be the normal assumption when continuous space is divided into grid cells)?

Yes this is what was written on l6. The point here was not this, but Eq. 6. To make it clearer, we have amended the phrase on l6 to “Within a given grid cell the associated mixing ratio is uniform.” It may sound trivial but these things help me to follow the rgumentation. “Thereby one uses the fact that“ has been removed as it is useless prosa. Also, it is not at all trivial anymore in the inversion, because model discretization leads to errors, which is touched on further below.

18) Page 5, line 18: Here a comment about the relative magnitude of m, n is needed. If $m < n$ the system is underdetermined and can only be solved by making additional assumptions. If $m > n$ the system is overdetermined and a least squares solution can be found.

We added. “Since $m > n$ the system is overdetermined, this means L in Eq. (7) cannot be inverted to arrive at c , but c has to be approximated. This is done here using a least square fitting procedure.” However, $m \gg n$, but not for all grids (at northern edge). So it is “mixed determined” Hence the issue with the non-uniqueness. We add this in the discussion (discussed at appropriate points below)

19) Page 5, line 19: What is the meaning of the double vertical lines, length of the vector ($m \times 1$ matrix)?

This is the Euclidean norm of the residuals as computed by Matlab. We added “normalized” before misfit.

20) Page 5, lines 22,23: The CO₂ flux will be derived in kg/second?

Yes, we use SI units. We have added “(in kg s^{-1})” just before Eq. 8.

21) Page 5, line 27: In 2016 the background CO₂ level reached 400 ppm, in industrialized areas probably even a bit more, why were 380 ppm used? what is the impact of this low bias on the derived fluxes?

We used 380 ppm as background CO₂ level since the air sample, which was collected far from the degassing area, gave this value, in accord with the background CO₂ content measured by Chiodini et al. a few years back in the same area (Chiodini et al., 2011, First 13C/12C isotopic characterisation of volcanic plume CO₂, Bull Volcanol., 73, 5:531-542, doi: 10.1007/s00445-010-

0423-2). We agree, the global average CO₂ level is now ~400 ppm but this level may be quite different from one location to another for various reasons (latitude, weather conditions, seasonal effects, anthropogenic contributions). Inside and around the Solfatara (e.g. the nearby crater of Astroni) there are many green areas, where the photosynthetic activity by plants likely causes the decrease in CO₂ levels compared to the more urbanized surroundings.

For discussion of the bias see 12.

22) Page 5, lines 27, 28: The statement about the "plume transport speed" is correct but misleading: since the scanned area is essentially the horizontal plane (I did not find information about a possible slope in the manuscript) the relevant component of u is the vertical component. Why not saying that?

We have added: "Since the scans were performed along the horizontal plane u refers to the vertical component of the plume transport speed."

23) Page 6, line 8, Eq. (10): What is the typical magnitude of the relative errors entering the Equation?

Typically, $\Delta u = 0.2$ m/s hence 20% relative error and 17% relative error (maximum) of in-plume XCO₂.

24) Page 6, line 21: It is confusing when the same letter (X) is used for two different quantities, the mixing ratio (XCO₂, av, in ppm, i.e. dimensionless) and the column integrated mixing ratio (XCO₂col in ppm, i.e. dimension of a length).

We agree. We now use Y for path amounts (ppm.m) and X for mixing ratios (ppm). This has been amended throughout the manuscript.

25) Page 6, lines 22,23: "Numerous wiggles indicate vigorous degassing activity ...". this appears to be in sharp contradiction to the "frozen plume" assumption (same page, line 20)?

No, the vigorous degassing activity refers to the location of potential vents. The formulation is a bit wishy-washy. We have replaced it with: "Numerous wiggles indicate widespread and heterogeneous degassing activity (...)"

26) Page 6, line 26: The meaning of the phrase "ranges and headings were converted to Cartesian coordinates" remains cryptic.

This relates to 27, so please see 27.

27) Page 6, line 29: What is the meaning of "associated coordinates" against which the XCO₂av data are plotted. XCO₂av are range averaged mixing ratios, the only coordinate available appears to be the scan angle (heading). So what is actually plotted in Fig 4?

Plotted are the XCO₂av against the associated x,y coordinates (after converting path length and angle to x,y coordinates). This was not indeed a bit cryptic. This has been clarified in the manuscript at p7, 15 : "Before inverting X_{CO₂}, the Y_{CO₂} and the associated rays were mapped onto a (x,y) grid as detailed in the method section. The coordinate system was chosen such that the instrument positions of all five scans were located on the y-axis (Fig. 1c). Table 1 shows an excerpt of the result of this procedure. In Fig. 4 the plot of X_{CO₂,av} versus $x_{j,k}$ and $y_{j,k}$ from Table 1 is

shown. It represents a semi-quantitative map indicating where high CO_2 concentrations are likely to be expected and thus contains useful a-priori information for the inversion.” and in the figure 4 caption: “Contour plot of Y_{CO_2} after mapping them onto (x,y) coordinates (which is the input to the inversion), divided by the range for all 627 beam paths (same as shown in Table 1 for first ray), which yields column averaged mixing ratios $X_{\text{CO}_2,av}$.” See also 16.

In addition, we added Figure 3, which summarizes all steps of the inversion: p6 l22: “Figure 3 summarizes all steps involved in the inversion.”

27) Page 7, first three paragraphs: The discussion about the inversion of the CO_2 column data into gridded mixing ratio values is cryptic and not convincing in many aspects:

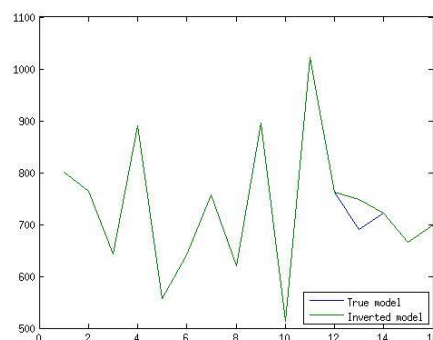
i) Did the runs of the LSQR algorithm with test data also include noise added to the test data? ii) It is stated that for $n > 36$ there were oscillations in the retrieved X_{CO_2} values, did this behaviour occur for all test distributions? How large were the oscillations? What was the influence of (artificial) noise on the oscillations? What were the criteria for judging the retrieval unacceptable? iii) For real data even $n > 16$ were reported to be a problem, but what was the problem, "unreasonable high" X_{CO_2} or oscillations or both? What was the reason for the different behaviour of the algorithm for test data and real data? iv) There is no information given on the error of the tomographic inversion, which may be huge! The large chi square (norm) of the inversion (around 18%, page 8, line 26) is an indication that the inversion has problems. Moreover, what about the uniqueness of the inversion, which was apparently not studied at all?

The point was to see if the LSQR solver is able to fit the model X_{CO_2} to realistic Y_{CO_2} (not random, but realistic and similar to what we expect looking at Fig. 4 and Tassi et al, 2013, Bagnato et al., 2014 (see References). Since this was the case and L was using the real ray coordinates the result of this synthetic inversion is quite meaningful.

The criteria to judge whether a model was good was simple. We know the order of magnitude of the X_{CO_2} and we know min and max. Based on this one can judge.

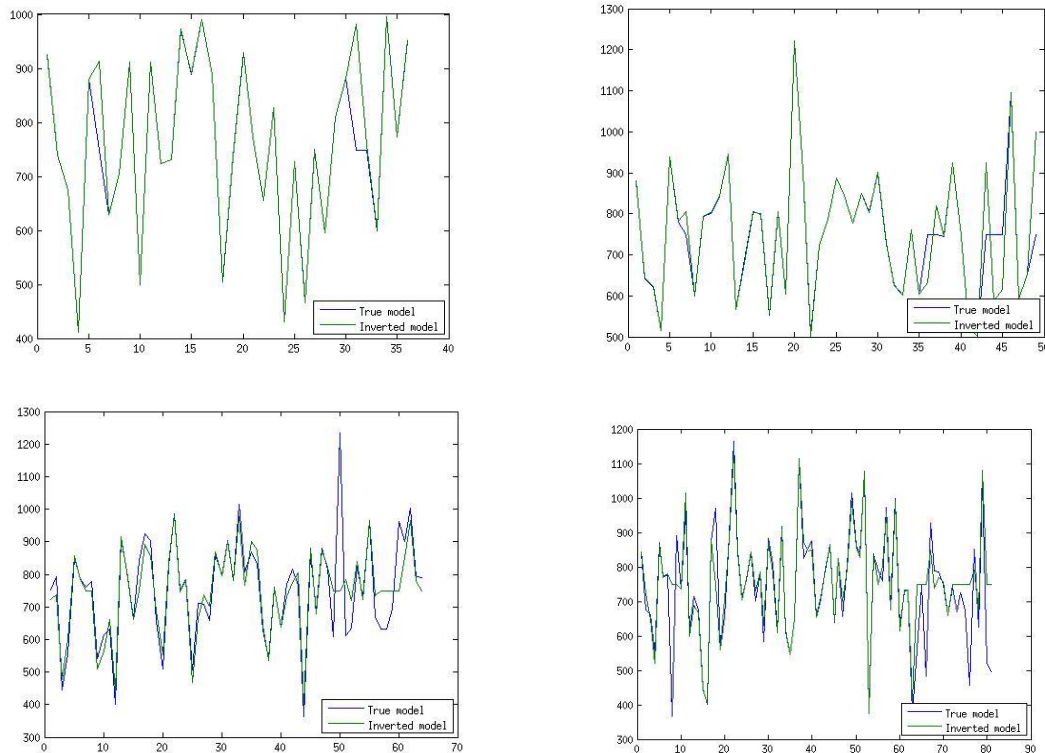
No, no noise was added to the test data. I'm not sure if I understand what noise means in that context and how it should be added. Perhaps you mean to try to perturb the synthetic Y_{CO_2} ?

I did a synthetic inversion test perturbing the Y_{CO_2} , which basically means using a different ad-hoc arrangement of the true X_{CO_2} . The result of a randomization of the distribution of the true X_{CO_2} is shown below and is quite similar. Apart from grid 13 (with poor ray coverage), the synthetic model is well recovered. We have qualitatively the same outcome for other distributions I tested, except that deviation from the real X_{CO_2} varies from distribution to distribution.

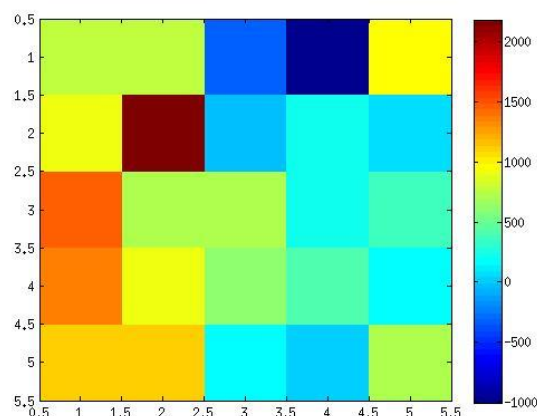


Below are some examples of synthetic inversion results with shuffled X_{CO_2} in the following order:

$n=36$, $n=49$, $n=64$, $n=81$. Failed recovery occurs for near edge grids, where ray coverage is poor or which are not intersected anymore by any rays. But all in all X_{CO_2} are well recovered. The last one shows the model from the manuscript, but with $n=64$ and the “oscillations”. Deviations are large, up to 200 ppm/1200 ppm. Seemingly the inversion copes better with the randomized distribution of X_{CO_2} . So “For $n > 36$ the inverted X_{CO_2} oscillated, that is, they were over and under shooting the true X_{CO_2} .” was not correct, but rather for $n > 49$. To answer your question, oscillations appear for all model arrangements after a certain n is superseded.

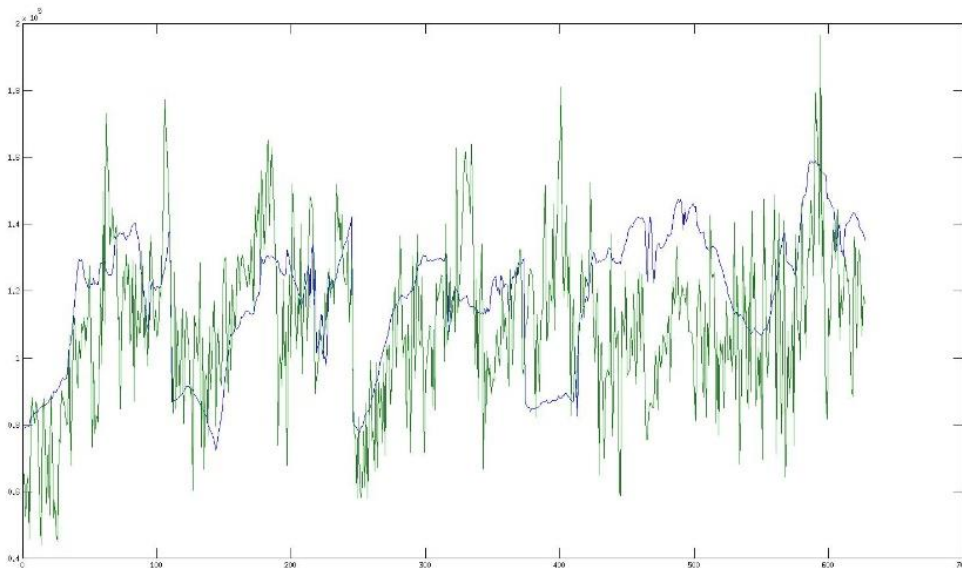


Inverting real data for $n > 16$ yields convergence, however, the inverted X_{CO_2} are unrealistic (negative X_{CO_2} or 0 for the grids at the edge with poor ray coverage or ray coverage with low angle diversity, such as in the figure below, grid 23,24 (3rd and 4th in top row), for instance). A criteria more meaningful to judge is actually the distribution of the inverted X_{CO_2} , which is not what one would expect.

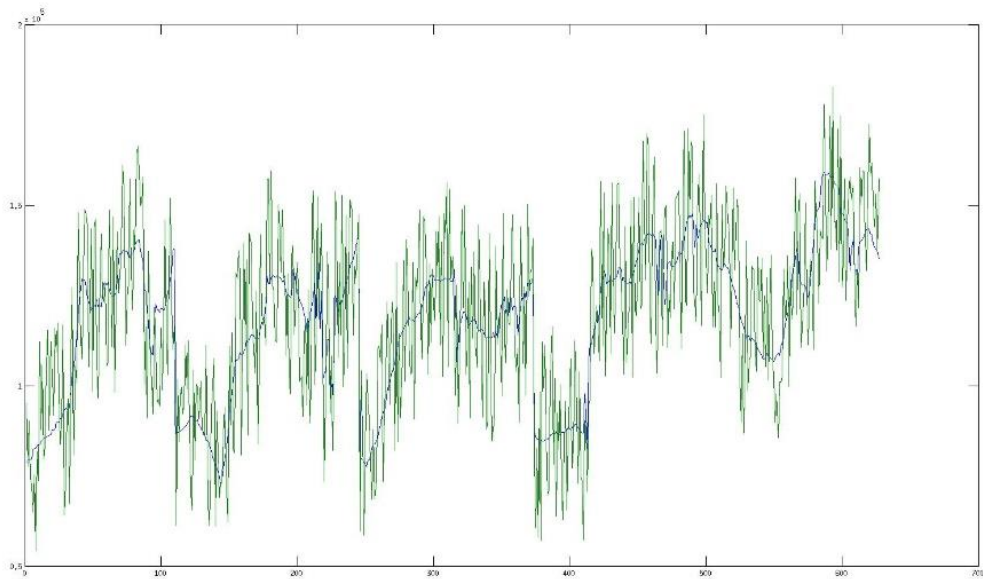


You helped us looking deeper into the issue of why the synthetic inversion better recovers the X_{CO_2} for larger n . I believe the reason is shown below, which shows the synthetic (blue) and the real data vector (green) (a from Eq. 7). It shows ppm.m versus ray number (627 in total). The real data vector has much higher frequency, which one may term noise in a mathematical sense (although it does not have to be associated with physical noise from the measurement). On p7 we added: “In reality the scanned area did not consist of 16 grids with homogeneous X_{CO_2} only, which leads to that spiky appearance of the real data vector. In our case a considerable part of that “noise” is due to the fact that actual fluctuations of the X_{CO_2} occurred on a faster time scale than the measurements of the 5 profiles (“frozen plume assumption). This leads to inconsistencies between the system of linear equations and hence difficulties to fit that data. “ Otherwise they are quite similar and one would not expect a different inversion result.

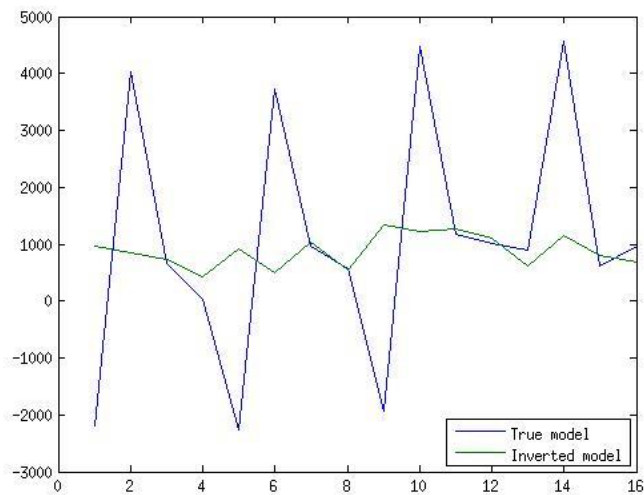
The “humps” in the figure below should somewhat resemble each other if the frozen plume assumption holds. It does so for the synthetic case (there are 5 somewhat similar but distorted humps, due to the different viewing angle of each scan). It is, however, partially the case also for the real data vector, at least for the first 4 scans. The high frequency components, however, differ a lot, suggesting short lived fluctuations on a small spatial scale.



I perturbed the synthetic data vector accordingly, which is shown below (green) along the original synthetic data (blue)

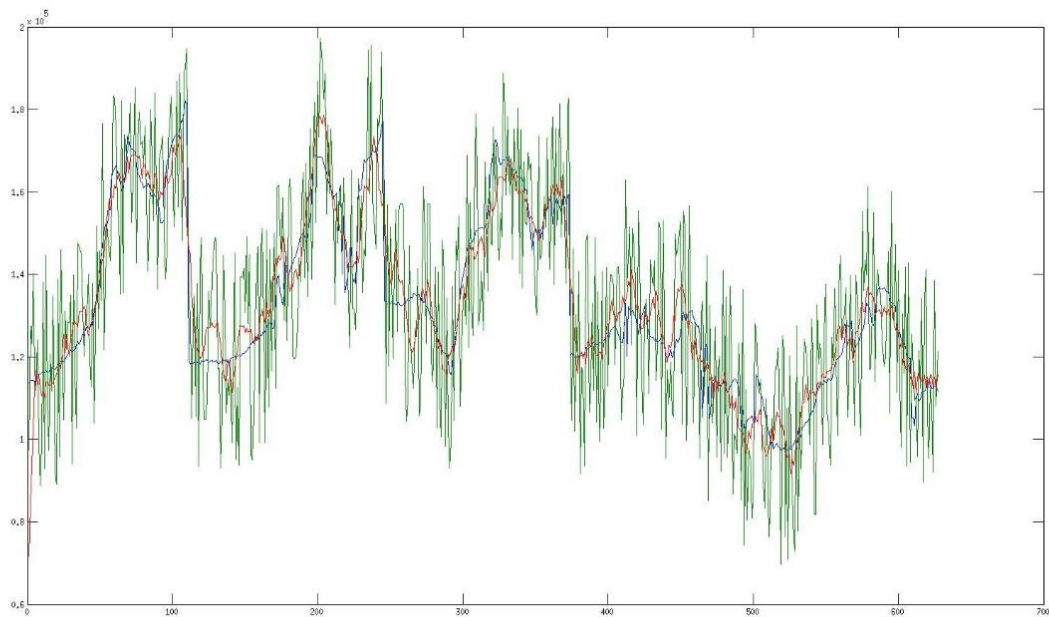


Here is the inversion result using that perturbed data (for n=16)

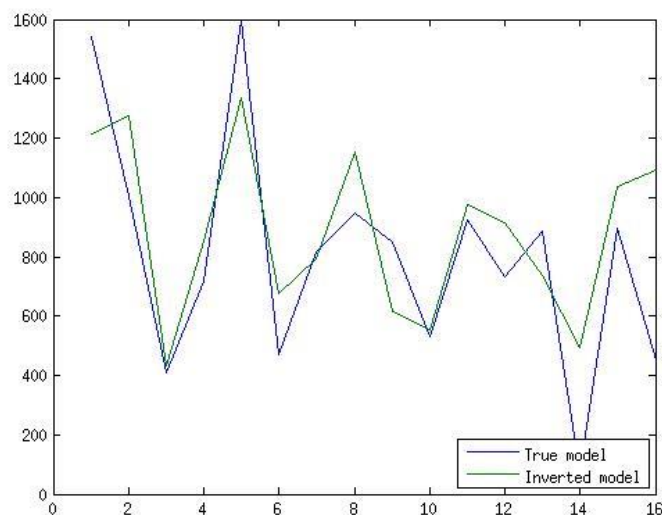


With those high frequency perturbations the synthetic data inversion struggles even more than the real data inversion, yielding oscillating XCO₂ (n=16 which yielded good results before (see above)). So I think that is clear now.

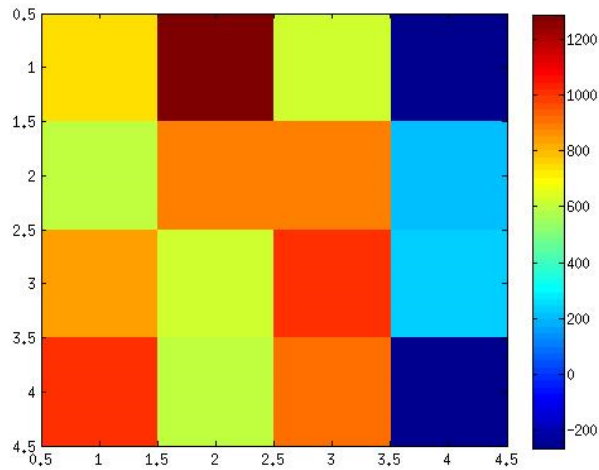
The next thing I did was to try to remove or at least reduce these oscillations. I found that since any kind of low pass operation (smoothing, filtering) alternates the magnitude of the lower frequency components of a , at some point the inversion fits the model to “falsified” data yielding poor recovery too, yet the mismatch is smaller than without any smoothing. So smoothing leads to a tradeoff. The best result was obtained with a simple moving average smoothing with small window size ($1/60$ of the length of a). Below the smoothed synthetic data (red), in blue the original, unperturbed data. However, this worked reasonably well for low n only, which explains why the real data inversion yields unreasonably low/high XCO_2 for $n > 16$. The tendency of oscillating XCO_2 increased with n , also for the synthetic inversions I performed.



Here is a result using that smoothed synthetic a for $n=4$:

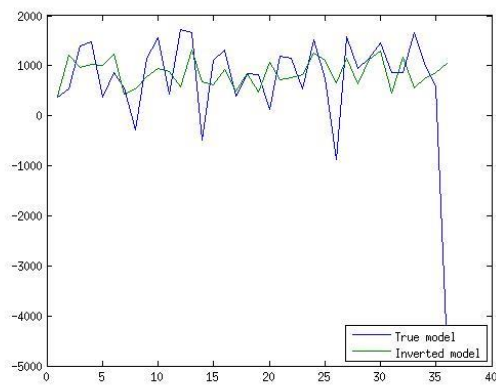


The XCO_2 is low (for some inversions negative) for grid cell at the right model edge (here 14 and 16, where there is poor ray coverage). More than 500 runs with random true model distributions yielded this kind of behavior. In can be observed in the real data inversion result too (using smoothed data):

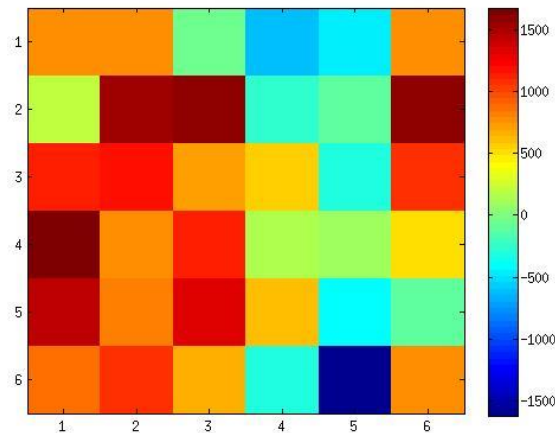


However, this is an improvement and a result one can work with. In fact, as for the synthetic inversion, near the right model edge the inverted model featured X_{CO_2} lower than encountered in the input data.

Here is a synthetic inversion result for $n=6$ (smoothed a) yielding similar poor recovery (legend reversed, green is true model):



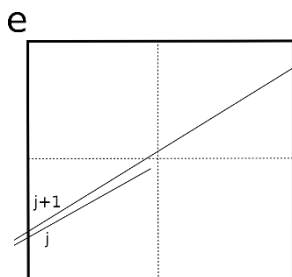
Here is the real data inversion result for $n=6$ with large oscillations, despite smoothing data vector a :



A possible reason why increasing n the inversion struggles is that while the problem is still overdetermined in the sense of ray coverage (at $n=64$ on average there are still 10 rays per grid cell), but they are not equally distributed. The near edge cells are traversed much less than the more central cells of the model. So the problem is actually mixed determined, leading to non-unique solutions. Most susceptible to oscillating X_{CO_2} should be the edge cells. In fact, this is what we can see in the inversion results. In summary, both synthetic and real data inversion behave very similar once the synthetic data is perturbed in a similar way the real data is. This suggests that performing an ensemble of synthetic inversions with varying distributions yields a meaningful error estimate of the real data inversion. Please see 28 for that.

We also found and added to the manuscript:

“Another contribution to the inconsistency of the system of linear equations is given by rays that are not traversing the edge grid cells due to the topography of the hard target (slope). This situation is illustrated in Fig. 6e (added to manuscript), shown below. This issue worsens upon increasing the number of grid cells.



Best results, that is, no oscillations, were obtained by selecting only 30% of the rays, and $n=16$. Every third ray and its corresponding Y_{CO_2} were used as input to the inversion. This measure effectively smooths the data vector without falsifying it and so decreases inconsistency of Eq. 7.

We have amended the manuscript according to these new tests and findings at the end of p 7 and the beginning of p8. See 33 for other corresponding changes in manuscript. Figure 7 has been added.

Your last question: We have tested different model discretizations before. With increasing number of grid points the model degrees of freedom increase and so does non-uniqueness. 4X4 was the most robust grid size, in the sense that this yielded an inversion result that matched the a-priori distribution of CO₂ (from previous independent studies) as well as the expected magnitudes of CO₂ concentrations. We had the luxury to know how the CO₂ concentration map should look like qualitatively. This yielded higher resolutions unsuitable, because it yielded unrealistic maps.

28) Page 7, last paragraph: In the introduction of the manuscript it is stated that high resolution CCO₂ distributions (multiplied with associated plume transport velocities) would yield superior data compared to using average XCO₂. However, can a 4 x 4 grid of CO₂ data really called "high resolution" in particular when keeping in mind that the tomographic inversion (LSQR algorithm) likely adds significant errors, further diminishing the theoretical advantage of spatially resolved XCO₂ data?

Perhaps I am missing something, but it is claimed nowhere in the manuscript that we were able to produce a high resolution tomography map of XCO₂. We do not even talk about high resolution (I could not find this word nowhere). The message (which obviously was not formulated clearly enough) was to try to use our data and see if we can get some 2D information out of it. In the introduction it reads: It would be very desirable, and this was the main motivation of this work, to have a 2-D map that at least contains the geometry of the anomalous CO₂ release, let aside precise CO₂ mixing ratios. Conclusion: Although the data was acquired in a way not ideal for tomography (one-sided) we obtain a meaningful result that is in line with independent data. I will try to make this more clear in the manuscript (p2 132) "It would be very desirable, and this was the motivation of this work, to use 1-D profiles of path amounts to reconstruct a 2-D map that at least contains the geometry of the anomalous CO₂ release, let aside precise CO₂ mixing ratios."

I tried to summarize the take home message of the paper in the conclusions by adding: (p11 1 26) "The one-sided acquisition geometry of the 1-D profiles, which were input to the inversion, was not ideal for a tomographic reconstruction and for $n > 16$ led to erroneous mixing ratios near the model edge, strongly limiting spatial resolution of the inverted model."

AND (p10 113): Furthermore, assumptions about the emission dynamics had to be made ("frozen" plume). Yet, the resulting map of X_{CO_2} was in satisfactory agreement with independent measurements of CO₂ mixing ratio.

Also, we try to formulate our conclusions more carefully:

In abstract we added: "The method may have important implications for measurements."

On p11 111: Future measurements of this type at Solfatara are envisaged, including a more systematic study, using a wider variety of viewing angles, which will allow a better assessment as to which extent this method is useful for one-sided tomography of highly non-isotropic CO₂ plumes in nature.

P11 131 Amended: "which indicates this tomography method to be potentially beneficial for scanning strongly" to indicate that this has to be verified in another experiment.

28) Page 7, last paragraph: What is the plume transport speed? Is it the vertical component of u?

It is the vertical component of u . “vertical component” added in the corresponding phrase. A reference to QueiBer et al., 2016, which details the retrieval method has been too.

28) Page 7, line 30: Do the stated errors include the errors of the tomographic inversion?

They do not. One could use the model covariance matrix. It is not straightforward and out of the scope of this work to obtain the model covariance matrix using the LSQR method. However, as a result of the discussion in 27, the synthetic data inversion yields a meaningful error estimate. Performing 1000 synthetic inversions and computing the absolute difference between true and recovered X_{CO_2} at each point yielded 16×1000 values with a mean of 373 ppm. We adopt this as a measure for the model standard deviation of the real data inversion (assuming it constant throughout the model). The numbers on p8 last paragraph and in the discussion as well as Eq. 10 are updated. We added (p8 l33): “Since the synthetic test inversions behave very similar to the real data inversion, to obtain a meaningful model uncertainty of the real data inversion 1000 synthetic inversions with random true models, drawn from a normal distribution using mean and standard deviation of the data presented in Figure 4 were carried out. Computing the absolute difference between true and recovered X_{CO_2} at each model grid point yielded 16×1000 values with a mean of 373 ppm. This was adopted as a measure for the model standard deviation of the real data inversion in Eq. 10 (assuming it constant throughout the model). This is the most dominant error, associated to relative uncertainties of the inverted X_{CO_2} between 34% and 90%.”

29) Page 8: line 2, figure 6: The Fig. is very confusing: How was the quadratic grid (Fig. 6a) mapped in the real shape of the area (Fig. 6c)? Were the squares distorted to match the real area? How? Also, the "smoothed" version of (Fig. 6a) shown in (Fig. 6b) does not appear to match. smoothing should smear out the maxima, but they appear to be shifted in (Fig. 6b) relative to (Fig. 6a), why?

We used Google Earth and trust Google’s algorithms to correctly project an overlay image onto the map (it is a function of Google Earth Software). That has been added in the Figure caption to make this clear: “To project the inverted model onto the map the function “overlay image” of Google Earth software has been used.” Fig. 6b is not a smoothed version of Fig. 6a, but the result of ordinary Kriging interpolation, as detailed in the manuscript text and in the figure caption.

29) Page 8: line 11: What is a "symmetric increase"?

The increase is symmetric with respect to the heading angle. “Symmetric” has been deleted as it is not important in that context. “Corresponds” replaced with “matches”, in the same phrase.

30) Page 8: lines 13, 14: The disagreement in peak positions is attributed to "physical" fluctuations in the CO₂ concentration. This appears to undermine the validity of the entire approach, effects like this will certainly give rise to large errors in the retrieved XCO₂, which of course, will propagate into the derived fluxes.

The inversion result (with all its normal problems) has been used to compute fluxes. Now, these fluxes are in line with the fluxes computed directly from the 1-D profiles. The inversion is adopted from Pedone et al. 2014. Note that they also used a 4x4 grid. So the approach is valid.

This is Earth science. The gap between our measurement capabilities and the complexity of real world natural phenomena (unlike in the laboratory) requires assumptions of that kind, which are very common when probing real world phenomena. That does not mean that the approach is undermined. Our inversion input data are coherent with in situ data and previous measurements as written in the discussion. Our inversion result is coherent with previous measurement results, as written in the discussion. For instance, scientists who are sitting somewhere outside in the field and

probe say a volcanic plume or a forest fire with an open path FTIR which has ~ 10 s integration time per point you need to make these kind of assumptions too. The alternative is to not do it and not get any result at all. But it is this kind of results that advance our methods eventually to a point where we are in the position to make less crude assumptions. In the laboratory, one designs an experiment and may optimize it until one gets the expected results and everything fits neatly. Outside the laboratory you may get only one chance, if that, and have to make the best out of the data. We will go there again and design an experiment just for this inversion and make it better. We already have written that in the discussion before.

31) Page 8: lines 19, 20: Lack of spatial matching underscores the observation stated in comment 30.

In the manuscript we could have expressed it more constructively: “The one-sided acquisition geometry of the 1-D profiles, which were input to the inversion, was not ideal for a tomographic reconstruction and led to erroneous mixing ratios near the model edge opposite to the instrument position and strongly limited spatial resolution of the inverted model. Furthermore, assumptions about the emission dynamics had to be made (“frozen” plume). Yet, the resulting map of X_{CO_2} was in satisfactory agreement with independent measurements of CO_2 mixing ratio.” Please see also 30.

32) Page 9: First two paragraphs: It appears that the large differences between the results of this study and other reported values are likely due to deficiencies of the method employed here. The attempt to bridge the gap is not convincing. For instance point sampling may miss spots of high CO_2 but equally likely miss spots of low CO_2 , so it is not obvious that the data should be low-biased.

Perhaps there is a misunderstanding here. The fluxes derived from the inversion procedure agree with the fluxes computed directly from the measured 1-D data and with fluxes measured previously. We are just saying that the values should be interpreted with care.

We also showed that the 2-D map is consistent with the 1-D input data (p9 last paragraph).

point sampling may miss spots of high CO_2 but equally likely miss spots of low CO_2 .

This is true if 50% of the area are covered with spots of high CO_2 . From what is known that appears not to be the case at Solfatara. Then, the CO_2 in these patches should be rather concentrated vs. the surrounding, but then this depends on the wind field... But it is true that this has to be changed. We have amended this: “If the area associated with lower CO_2 concentration was larger than the area with very high CO_2 concentration, point sampling may have missed degassing activity in between the measurement points and so tended to yield lower flux values”. It is somewhat speculative, but this is OK since it is written in the discussion section. Also, there has been a general increase in flux at Solfatara, which is what is written below on p9.

Our flux value is by no means out of line. In fact, the last phrase of that paragraph suggests that our flux is in line with an increase in degassing rate:

The total CO_2 flux of the DDS (the degassing zone, which comprises the Solfatara crater, the Pisciarelli fumaroles and some areas with smaller degassing strength nearby), was estimated to be 1500 t/day in 2001 (Chiodini et al., 2001, CO_2 degassing and energy released at Solfatara volcano, Campi Flegrei). So our flux value is in line with that figure, keeping in mind that the emission rate increased significantly since then.

The corresponding phrases have been amended (p10 l30): The magnitude of the retrieved flux of this work equals the total CO_2 flux of DDS (diffuse degassing structure, which encompasses

Solfatara crater, the Pisciarelli fumaroles and the area around Solfatara crater) reported by Granieri et al. (2003), however, 13 years prior to this study, when emission rates were 1.09^{13} (or 3) times lower. A very rough extrapolation of the 1465 tons day⁻¹ obtained here to the whole of Solfatara crater, that is, by assuming a constant flux per unit area (Queißer et al., 2016) would yield a flux between 2400 and 4700 tons day⁻¹. This makes 1465 tons day⁻¹ a coherent figure.

33) Page 9, lines 23, 24: Why should the inversion problem become non linear? After all tomographic inversions are linear transformations (see also Eq. (7), which is clearly a linear equation).

You are right that is misleading. The problem is linear. That was incorrect. What was meant here was the non-uniqueness. Not all tomographic inversions are linear, however.

We have changed “increases the non-linearity of the inverse problem” to “increases the non-uniqueness of the inverse problem“

We misinterpreted the issue of poor recovery of XCO₂ (see for example 27). Consequently we deleted: “Generally, a viable strategy to tackle non-linearity in situations like that is a gradual introduction of non-linearity, such as by splitting up the inversion into sub-steps, using a starting model close enough to the true solution at each step (Queißer et al., 2012). With each increase in sub-step, the starting model contains more small-scale information. This approach was tested in the real data inversion. Starting with $n = 4$ grid cells, the inversion result was interpolated, smoothed and used as the starting model for the inversion with $(n_x + 1)^2$ grid cells. At $n = 25$ the location of the peak XCO₂ were in strong disagreement with the LICOR data, indicating that the inversion was trapped in a local minimum. A similar outcome was obtained by reducing the number of rays used for the inversion (using every 2nd up to every 10th ray). “

Further related changes were:

(p10 l22): changed “This is not ideal for any inversion technique as it makes the inverse problem highly non-linear with a non-unique solution, meaning that many models may explain the observed data equally well.” To “As evinced above, this was not ideal for any inversion technique as it makes the inverse problem mixed determined, leading to a non-unique solution, meaning that many models may explain the observed data equally well.”

P10 l26: “The inverted model is missing small-scale features, since to linearize the inversion the grid spacing had to be rather coarse.” To “Due to the coarse grid spacing the inverted model is missing small-scale features. This was necessary to exclude non-unique solutions which arose at grid numbers $n > 16$.”

Other changes made by the authors

Figure 4 caption: added “For display purposes” to l3 of caption

P3 l22: “the key quantity to be measured” added

P5, l11: added ” (rows of L)”

P5 l30: Added “Ordinary Kriging interpolation may then be applied to obtain a higher resolution estimate of the map.”

P6 119 added “measurement precision“

P6 120: added “and $\sigma_{X_{CO_2}}$ is an estimate of the error of the inverted model”

P7 113: added “using Eq. (7)”

Added Reference (p8 110): Zhang., Y., Gulliksson, M., Hernandez Bennetts, and V. M., Schaffer., E.: Reconstructing gas distribution maps via an adaptive sparse regularization algorithm, Inverse Problems in Science and Engineering, 24, 1186-1204, 2016.

P 8 123: Deleted “. Since zones with poor ray coverage were prone to inversion artifacts (see Fig. 4c) zones without ray coverage were excluded from integration.” As this was not the case anymore.

P8 124 Added “The inverted model is shown in Figure 8a.”

P8 132 Added “Queißer et al., 2016“

Figure 8 caption: Added: “Moreover, measured column integrated mixing ratios were below 1500 ppm, so there are X_{CO_2} of 1500 ppm expected in the inversion result”. AND “while the straight lines outline the grid.”

Figure 8 adapted to new inversion result, see discussion in 27.

P9 121. Deleted (and thus degree of non-linearity), see 33, Phrase changed to “Encouragingly, this is a persistent feature in different inversions performed with different number of beam paths, smoothing of input data and underpins that it is real”

P10 11 Added “(“frozen” plume approximation)”

P10 12 Removed “The plume was assumed to be “frozen”, but the measurement duration of 142 min was certainly larger than the time scale of alterations in the dispersion pattern of the plume” and added “measurement duration of 142 min” to results on p8, 12 where this issue is already discussed.

Added “as evinced in the result section”

P10 14 added “and temporal”

P10 14: Added: Note that due to the non-uniqueness of the problem a lower misfit does not imply that the inverted model is closer to the “true” model.

And “Although being close to the expected distribution, the mismatch is therefore likely due to a non-unique realization of the model, due to poor ray coverage for grid 16, which is partly the zone containing the main vents.”

P10 124 Removed as is redundant: “Note that disagreement with the flux result from the 2-D map may partly be due to the frozen plume assumption, since this assumption is better fulfilled for the acquisition of a single 1-D profile, which takes much less time. Future scans shall thus be acquired with higher scan velocity or from further away.

P10: To our knowledge, all former studies except one (Pedone et al., 2014) inferred X_{CO_2} and hence CO_2 fluxes from a grid of point measurements. If we assume that the area associated with lower

CO₂ concentration is larger than the area with very high CO₂ concentration, point sampling may have missed degassing activity in between the measurement points and so tended to yield lower flux values. Spatially comprehensive sounding by moved further below as this is not the priority reason for different flux values.

P10 I30 added: “which encompasses the area around Solfatara crater”

P10 I33 The XCO₂ are displaced from the expected area (in addition by a relatively small amount of 17 m). This does not change the magnitude and hence the flux of the scanned area, as demonstrated just before with the estimated flux of 390 tons/day that agrees with previous measurements. Therefore and because this reasoning confuse the reader we removed “However, as mentioned before, CO₂ from the main vents mixes with surrounding volcanic CO₂ and furthermore the scans focused on the area south of the main vents (poor ray coverage at BN and BG). So this value should be interpreted with care. It deems to be reasonable to exclude the zone of high anomalous degassing in the north of the 2-D map, which leads to a flux of 675 ± 175 tons/day, representing any degassing activity (vented and diffuse) within the investigated area, excluding the main vent area (BN and BG).”

P 11, Deleted last phrase of discussion” The outcome indicates this method to be particularly useful for future measurement campaigns using hard target DIAL to scan volcanic plumes from an aircraft or similar acquisition geometries sensing other types of gas emission.“ as is redundant (mentioned in conclusions)

Added grid in Fig. 8b and in caption of Fig. 8: while the straight lines outline the grid AND Moreover, measured column integrated mixing ratios were below 1500 ppm, so there are X_{CO_2} of 1500 ppm expected in the inversion result.
AND (interpolated grid size is 3.75 by 4.38 m)

2-D tomography of volcanic CO₂ from scanning hard target differential absorption LIDAR: The case of Solfatara, Campi Flegrei (Italy)

Manuel Quei er^{1,*}, Domenico Granieri², Mike Burton¹

5 ^{1,*}School of Earth, Atmospheric and Environmental Sciences, University of Manchester, Oxford Road, Manchester M139PL, UK

²Istituto Nazionale di Geofisica e Vulcanologia (INGV), Sezione di Pisa, 50126 Pisa, Italy

Correspondence to: Manuel Quei er (manuel.queisser@manchester.ac.uk), Tel.: +44(0)161 2750778, Fax.: +44(0)161 306 9361

10

Abstract. Solfatara is part of the active volcanic zone of Campi Flegrei (Italy), a densely populated urban area where ground uplift and increasing ground temperature are observed, connected with rising rates of CO₂ emission. A major pathway of CO₂ release at Campi Flegrei is diffuse soil degassing, and therefore quantifying diffuse CO₂ emission rates is of vital interest. Conventional in-situ probing of soil gas emissions with accumulation chambers is accurate over a small footprint but requires significant time and effort to cover large areas. An alternative approach is differential absorption LIDAR, which allows for a fast and spatially integrated measurement. Here, a portable hard-target differential absorption LIDAR has been used to acquire horizontal 1-D profiles of column integrated CO₂ concentration at the Solfatara crater. To capture the non-isotropic nature of the diffuse degassing activity, a 2-D tomographic map of the CO₂ distribution has been inverted from the 1-D profiles. The scan was performed one-sided, which is unfavorable for the inverse problem. Nonetheless, the result is in agreement with independent measurements and furthermore confirms an area of anomalous CO₂ degassing along the eastern edge as well as the center of the Solfatara crater. The method may have important implications for measurements of degassing features that can only be accessed from limited angles, such as airborne sensing of volcanic plumes. CO₂ fluxes retrieved from the 2-D map are comparable, but modestly higher than emission rates from previous studies, perhaps reflecting a more integrated measurement.

25

1 Introduction

Subaerial volcanoes emit a variety of gaseous species, dominated by water vapor and CO₂, and aerosols. Originating from exsolution processes that may take place deep in the crust due to the low solubility of CO₂ in magmas, volcanic CO₂ is a powerful tracer for magmatic recharge and ascent processes (Burton et al., 2013; Frezzotti et al., 2014; Chiodini et al., 2015; La Spina et al., 2015). Measuring volcanic CO₂ emission rates is therefore also a feasible pathway towards improved

forecasting of volcanic activity, such as seismicity or eruptions (Petrazzuoli et al., 1999; Carapezza et al. 2004; Aiuppa et al., 2011). Unfortunately, magmatic CO₂ is not only released actively via vents such as the volcano mouth, but also diffusively via soil or flank degassing (Baubron et al., 1991; Hards, 2005; Chiodini et al., 2007). In addition, in most cases the volcanic CO₂ signal is modest compared with ambient concentrations (Burton et al., 2013) and quickly diluted into the atmosphere. A common approach to determine the magmatic CO₂ flux is based on a gridded sampling of the CO₂ distribution in the volcanic plume itself (Gerlach et al., 1997; Lewicki et al., 2005; Diaz et al., 2010; Lee et al., 2016) from which 2-D CO₂ concentration maps are retrieved by secondary data processing, such as statistical methods (Lewicki et al., 2005; McGee et al., 2008) and dispersion modeling (Aiuppa et al., 2013; Granieri et al., 2014). Integrating the CO₂ concentrations over the cross sectional plume area and multiplying the result with the transport speed perpendicular to the cross section yields CO₂ fluxes. The in situ method has two drawbacks. Firstly, it may be dangerous to perform in situ measurements from within the volcanic plume (e.g. due to toxic gases or low visibility near the crater mouth). Secondly, in situ methods allow for a very accurate estimation of CO₂ concentration, but only in the vicinity of the measurement point, potentially missing significant contributions from in between the measurement points.

Remote sensing techniques (see Platt et al., 2015 for overview of state-of-the-art), notably active remote sensing platforms, including differential absorption LIDAR (DIAL) and spectrometers (Menzies and Chahine, 1974; Weibring et al., 1998; Koch et al., 2004; Kameyama et al., 2009) acquire columns of range resolved (Sakaizawa et al., 2009; Aiuppa et al., 2015) or column averaged (Amediek et al., 2008; Kameyama et al., 2009) CO₂ concentrations. They provide a powerful tool to overcome the aforementioned drawbacks of in situ measurement techniques by offering a faster, safer and comprehensive acquisition (spatial coverage yields inclusive CO₂ concentration profiles). Moreover, there is no need for receivers or retroreflectors at the opposite end of the measurement column, which increases not only flexibility and timeliness of the acquisition, but is crucial for some measurements, including airborne or spaceborne acquisitions.

Active remote sensing platforms based on hard target DIAL (topographic target DIAL) using continuous wave lasers can be made compact, rugged and portable, which is desirable for platform independent measurement of atmospheric CO₂, be it ground based or air-borne (Sakaizawa et al., 2013; Queißer et al., 2015a). Yet, the drawback compared with “traditional”, pulsed DIAL is that no range resolved CO₂ concentrations are measured, but column densities (in m⁻²) or, as in this work, path length concentration products (called “path amount” hereafter, in ppm.m). Hence, during a scanning measurement, no 2-D concentration maps are obtained, but 1-D profiles of path amounts, that is, values of path amounts versus scanning angle. Using these profiles to determine CO₂ fluxes is straightforward only for gas plumes for which a homogeneous cross section can be assumed (Galle et al., 2010). However, particularly diffuse degassing activities are often not associated with homogeneous, but an unknown CO₂ distribution within the scanned plume cross section. Therefore, the assumption of homogenous CO₂ distribution may lead to under or overestimated CO₂ fluxes when probed from different directions, since path amounts are measured, which are associated with path averaged CO₂ concentrations. It would be very desirable, and this was the motivation of this work, to use the 1-D profiles of path amounts to reconstruct a 2-D map that at least contains the geometry of the anomalous CO₂ release, let aside precise CO₂ mixing ratios. This would allow to geometrically correct the

fluxes derived from CO₂ path amounts delivered by hard target DIAL systems. Note that tomographic reconstructions of volcanic gas plumes have already been performed, however, for SO₂ and using passive remote sensing techniques (Kazahaya et al., 2008; Wright et al., 2008; Johansson et al., 2009).

The study was focusing on a zone of diffuse degassing of magmatic CO₂ within the Solfatara crater (Italy) reported previously (e.g. Bagnato et al., 2014). Solfatara is a fumarolic field and part of the active volcanic area of Campi Flegrei (CF, Fig. 1). CF is a nested caldera resulting from two large collapses, the last one ~15 ka ago (Scarpato et al., 1993). CF is in direct vicinity to the metropolis of Naples and thus a direct threat to millions of residents. Thanks to its accessibility and strong CO₂ degassing Solfatara provides almost a model like volcano, a natural laboratory, to test new sensing approaches. On the other hand, it is part of one of the most dangerous volcanic zones in the world, showing ground uplift coupled with seismic activity with magma degassing likely having a significant role in triggering unrest (Chiodini et al., 2010). Solfatara therefore merits particular monitoring efforts and any new results on observables, may they stem from well-tried or new methods, are of direct importance to understand the fate of this active volcanic system.

2 Methods

2.1 Measuring 1-D profiles of CO₂ path amounts

The CO₂DIAL (Fig. 2) is an active remote sensing platform based on the differential absorption LIDAR principle (Koch et al., 2004; Amediek et al., 2008). It is a further development of the portable instrument described in Queißer et al. (2015a, 2015b). Specifics about the instrument and how CO₂ path amounts were retrieved are explained in detail in Queißer et al., 2016. Here, only a brief overview is given. By taking the ratio of the optical powers associated with the received signals for the wavelengths coinciding with an absorption line of CO₂ and the wavelength at the line edge, λ_{ON} and λ_{OFF} , respectively, one arrives at

$$2 \int_0^R dr \Delta\sigma(r) N_{CO_2}(r) = -\ln \left(\frac{P(\lambda_{ON})P(\lambda_{OFF})_{ref}}{P(\lambda_{OFF})P(\lambda_{ON})_{ref}} \right), \quad (1)$$

$\equiv \Delta\tau$

which is the differential optical depth $\Delta\tau$, the key quantity to be measured. N_{CO_2} is the CO₂ number density, R is the range, i.e. the distance between the instrument and the hard target, $\Delta\sigma$ is the difference between the molecular absorption cross sections of CO₂ associated with λ_{ON} and λ_{OFF} , $P(\lambda)$ is the received (“science”) and $P(\lambda)_{ref}$ the transmitted optical power (“reference”). The latter is measured as a reference to normalize fluctuations of the transmitted power. The normalized optical power in Eq. (1) is referred to as grand ratio (GR),

$$GR = \frac{P(\lambda_{ON})P(\lambda_{OFF})_{ref}}{P(\lambda_{OFF})P(\lambda_{ON})_{ref}} \quad (2)$$

The two distributed feedback (DFB) fiber seed lasers emit at $\lambda_{ON}=1572.992$ nm and $\lambda_{OFF}=1573.173$ nm (Rothman et al., 2013). To be able to easily reject background noise (such as solar background) lock-in detection is used. Consequently, both seed laser beams (for λ_{ON} and λ_{OFF}) are amplitude modulated using two LiNbO₃ electro-optical modulators (EOM) at slightly

different sine tones near 5 kHz and simultaneously amplified by an Erbium doped fiber amplifier (EDFA) before being **simultaneously** transmitted. The transmitted optical power can be adjusted between ~80 mW and a maximum of 1.5 W. A glass wedge scatters a fraction of the transmitted light into an integrating sphere where the reference detector is mounted, which measures $P(\lambda_{ON})$ and $P(\lambda_{OFF})$. The transmitted light is diffusively backscattered by a hard target, which can be any surface located up to ~2000 m away from the instrument, and is received by a 200 mm diameter Schmidt-Cassegrain Telescope with a focal length of 1950 mm and field of view of . Typically the received optical power is a couple of nW at a bandwidth integrated noise of ~1 pW (root mean squared noise equivalent power). The analog to digital converter (ADC) operates at 250 kSamples s^{-1} and has a resolution of 16-bit. The integration time per scan angle was set to 4000 EOM modulation periods, which corresponds to data chunks of length 784 ms (integration time) for both science and reference channel. Each of these four chunks of data is demodulated using a digital lock-in routine following Dobler et al. (2013). After the lock-in operation one arrives at four DC signals, associated with the optical powers $P(\lambda_{ON})$, $P(\lambda_{OFF})$, $P(\lambda_{ON})_{ref}$ and $P(\lambda_{OFF})_{ref}$. $\Delta\tau$ is calculated using the right hand side of Eq. (1), after taking the mean of each of the four signals. **However, to retrieve CO₂ path amounts the left hand side of Eq. (1) was not used.** Instead, to account for the instrumental offset of $\Delta\tau$, prior to scanning the volcanic plume, values of $\Delta\tau$ were acquired for different R in the ambient atmosphere (Queißer et al., 2016). The points were used to fit a calibration curve. The ordinate at $R=0$ gave the instrumental offset. The calibration curve was also used to convert the measured in-plume $\Delta\tau$ to CO₂ path amounts Y_{CO_2} (in ppm.m). Column averaged CO₂ mixing ratios $X_{CO_2,av}$ (in ppm) were obtained by dividing path amounts by R . The range was measured by an onboard range finder (DLEM, Jenoptik, Germany), based on a 1550 nm LIDAR with pulse energy of 500 μ J and accuracy <1 m. By pivoting the receiver/transmitter unit using a step motor values for Y_{CO_2} (or $X_{CO_2,av}$) per heading were attained, and hence 1-D profiles.

20 The precision of the column averaged CO₂ mixing ratio was evaluated as

$$\left(\frac{\Delta X_{CO_2,av}}{X_{CO_2,av}}\right)^2 = SNR^{-2} + \left(\frac{\sigma_R}{\langle R \rangle}\right)^2 + \delta_{speckle}^2, \quad (3)$$

with the signal-to-noise-ratio (SNR)

$$SNR = \left[\frac{\sigma_{GR}}{\langle GR \rangle} \frac{1}{\ln(\langle GR \rangle)}\right]^{-1}, \quad (4)$$

where $\langle GR \rangle$ and σ_{GR} are the mean and standard deviation of the grand ratio, respectively. They were estimated from time series acquired at fixed angles in between the scans at CF. The SNR accounts for all noise sources occurring during acquisition, including instrumental noise, non-stationary baseline drift, solar background noise, atmospheric noise (mostly air turbulence) and perturbation by aerosol scattering (e.g. condensed water vapor). The second term depicts the relative range uncertainty (standard deviation of ranges σ_R over mean of ranges $\langle R \rangle$) which is typically ~1 m. The relative uncertainty due to hard target speckle was estimated as (MacKerrow et al., 1997)

$$30 \quad \delta_{speckle} = \frac{1.22\lambda_{OFF}R}{D\xi}, \quad (5)$$

where D is the spot diameter on the hard target (in m) and ξ is the dimension of the telescope field of view (in m) on the hard target.

2.2 Reconstructing a 2-D map of CO₂ mixing ratios

The goal is to obtain CO₂ mixing ratios (X_{CO_2} , in ppm) at a given point (x, y). The region of interest (area bounding the scans) was divided into grid cells with length Δx (in x direction) and Δy (in y direction). Within a given grid cell the associated mixing ratio is uniform. X_{CO_2} were inferred from the measured Y_{CO_2} using an inverse technique following Pedone et al. (2014).

- 5 The CO₂ path amount is associated with the product of a range segment and the (uniform) CO₂ mixing ratio X_{CO_2} along that range segment. For a given beam path and heading angle (hereafter also referred to as ray) and for n grid cells traversed by the ray this can be written as

$$\sum_{i=1}^n r_i X_{CO_2,i} = Y_{CO_2}, \quad (6)$$

- where r_i depicts the length of the ray segment in grid cell i ($\sum_{i=1}^n r_i = R$). $X_{CO_2,i}$ is the (unknown) CO₂ mixing ratio within grid cell i (in ppm). Including all rays, one arrives at a system of linear equations, which can be written as

$$Lc = a, \quad (7)$$

- where L is a $m \times n$ matrix, called geometry matrix, containing the length of all m paths (rows of L) for all n grid cells. To be able to apply Eq. (7) to the measured Y_{CO_2} , the associated rays were mapped onto (x, y) coordinates using $x_{j,k} = r_{j,k} \cos \Delta\varphi_j$ and $y_{j,k} = r_{j,k} \sin \Delta\varphi_j$. φ_j is the cumulative heading angle of the j^{th} ray determined from the scanning angular velocity and the time interval between the rays retrieved from the time stamps of the data. For a given ray, $r_{j,k}$ is the k^{th} path length increment, such that $\sum_{k=1}^N r_k = R_j$. N is chosen such that adjacent x_j and y_j were no more than ~ 1 m apart. Since the $\Delta\varphi_i$ are not absolute angles, but relative to the first ray the $x_{j,k}$ and $y_{j,k}$ were rotated to match the world coordinate system, i.e. rotated such that the first ray's (x, y) coordinates match the real world ray trajectory. This was performed using the well know rotation matrix with a rotation angle, which is the angle between the first ray and the x -axis. The Y_{CO_2} versus the resulting (x, y) coordinates formed the inversion input file (see Table 1 for an example). From the data in that input file an algorithm built the geometry matrix L by associating the (x, y) coordinates with the n model grid cells. c is a $n \times 1$ matrix containing uniform X_{CO_2} per grid cell and is the desired quantity to be inverted. a is a $m \times 1$ matrix containing the measured (observed) Y_{CO_2} for each ray, retrieved from the inversion input file. For simplicity, $n_x = n_y$, where n_x, n_y are the number of grid cells in x - and y -direction, respectively. Thus, $n = n_x^2$.

- 25 Since $m \gg n$ the system is overdetermined. This means L in Eq. (7) cannot be inverted to arrive at c , but c has to be approximated. This is done here using a least square fitting procedure. To solve Eq. (7) for c a least square solver, the MATLAB LSQR routine, was used. The algorithm iteratively seeks values for c , which minimize the normalized misfit $\|a - Lc\|$. Therefore, c represents a model with a maximized likelihood of explaining the observed data a . By reshaping c into the measurement 2-D grid a 2-D map was obtained. Ordinary Kriging interpolation (Oliver, 1996) may then be applied to obtain a higher resolution estimate of the map.

2.3 CO₂ flux retrieval

From the inverted 2-D map of X_{CO_2} the CO₂ flux (in kg s⁻¹) was computed as

$$\phi_{CO_2} = 10^{-6} u N_{air} \frac{M_{CO_2}}{N_A} \iint_{plume} dx dy X_{CO_2,pl}(x, y) \quad (8)$$

5 where $X_{CO_2,pl}$ are the inverted, background corrected CO₂ mixing ratios computed as

$$X_{CO_2,pl}(x, y) = X_{CO_2}(x, y) - X_{CO_2,bg}, \quad (9)$$

where $X_{CO_2,bg} = 380$ ppm is the background CO₂ mixing ratio at Solfatara measured in situ from an air sample, which was collected far from the degassing area, in accordance with Chiodini et al. (2011). The global average CO₂ level is now ~400 ppm but this level may be quite different from one location to another for various reasons (latitude, weather conditions, seasonal effects, anthropogenic contributions). Inside and around the Solfatara there are many green areas (e.g. the nearby crater of Astroni), where the photosynthetic activity by plants likely causes the decrease in CO₂ levels compared to the more urbanized surroundings. u is the magnitude of the component of the plume transport speed perpendicular to the scanned cross section (in m s⁻¹). Since the scans were performed along the horizontal plane u refers to the vertical component of the plume transport speed. N_{air} is the number density of air (in m⁻³), computed using meteorological data (pressure, temperature, humidity) acquired by a portable meteorological station close to the instrument. M_{CO_2} is the molar mass of CO₂ (in kg mol⁻¹) and N_A is Avogadro's constant (in mol⁻¹).

The plume transport speed was evaluated from digital video footage acquired during the measurement (Queißer et al., 2016), employing a video analysis program (Tracker from Open Source Physics). Condensed water vapor aerosol emitted by various vents in the region of interest was assumed to propagate with the same velocity as the volcanic CO₂. At a given video frame a pixel was fixed and the calibrated propagated distance (in pixels) was measured as the video proceeded. Since the frame rate of the video was known (30 frames per second), the speed by which the tracked point and hence a parcel of gas was transported could be estimated.

The relative error of the CO₂ flux was estimated as

$$\left(\frac{\Delta \phi_{CO_2}}{\phi_{CO_2}} \right)^2 = \left(\frac{\Delta u}{u} \right)^2 + \left(\frac{\iint_{plume} dx dy \Delta X_{CO_2,pl}(x,y)}{\iint_{plume} dx dy X_{CO_2,pl}(x,y)} \right)^2 + \left(\frac{\iint_{plume} dx dy \sigma_{X_{CO_2}}}{\iint_{plume} dx dy X_{CO_2}(x,y)} \right)^2 \quad (10)$$

25 where Δu is the absolute uncertainty of the plume speed, $\Delta X_{CO_2,pl}$ is the absolute error of the CO₂ mixing ratio (measurement precision) at a given point within the integrated area and $\sigma_{X_{CO_2}}$ is an estimate of the error of the inverted model. Figure 3 summarizes all main steps that were involved in the methods to retrieve the flux.

3 Results

The experiment took place on 4 March 2016 inside the crater of Solfatara (Fig. 1) and was focusing on the diffuse CO₂ release alongside the Solfatara crater edge, located south of the main vents Bocca Nuova (BN) and Bocca Grande (BG), although they were included in the scans. Elevated CO₂ mixing ratios, up to 1500 ppm at places, could be affirmed by means of in situ measurements using a LICOR CO₂ analyzer with 4% accuracy. The LICOR analyzer was measuring at the same height as the propagation height of the laser beam (ca. 2 m above ground). Due to logistical constraints the in situ measurements could only be measured the day before the experiment. Five scans were performed between 9:35 and 11:57 LT (duration 142 min) from five different locations with a total of $m = 627$ beam paths (rays), which are shown along with the respective five instrument locations in Fig 1c. It is assumed that during the complete acquisition the CO₂ distribution did not change (“frozen plume”). For each scan and for each heading differential optical depths $\Delta\tau$ have been retrieved and converted into Y_{CO_2} (and $X_{CO_2,av}$), as detailed in the method section. The resulting 1-D profiles of CO₂ path amounts are shown in Fig. 3. Numerous wiggles indicate widespread and heterogeneous degassing activity, suggesting diffuse degassing or CO₂ advected by local wind eddies. In addition, there are symmetric features, such as around 26° in Fig. 3a, which appeared in scans carried out prior to the experiment and the day before, thus suggesting vented degassing activity. The angular scanning velocity was 2.1 mrad s⁻¹, associated with an angular resolution of 1.65 mrad, which corresponds to a lateral resolution of around 24 cm between points in Fig. 3.

Before inverting X_{CO_2} , the Y_{CO_2} and the associated rays were mapped onto a (x,y) grid as detailed in the method section. The coordinate system was chosen such that the instrument positions of all five scans were located on the y-axis (Fig. 1c). Table 1 shows an excerpt of the result of this procedure. Figure 5 shows the plot of $X_{CO_2,av}$ versus $x_{j,k}$ and $y_{j,k}$ (shown in Table 1). It represents a semi-quantitative map, indicating where high CO₂ concentrations are likely to be expected and thus contains useful a-priori information for the inversion.

The LSQR algorithm was tested using a synthetic, realistic scenario. Synthetic data Y_{CO_2} were generated from a true model comprising of known X_{CO_2} at each grid point using Eq. (7) and the real geometry matrix L , which contained the actual instrument positions and measured ranges. X_{CO_2} of the true model were starting at 380 ppm at grid 1 and increasing by 60 ppm per increase in grid number (Fig. 6a). The inversion result is shown in Figs. 6b and 6c. By running the inversion with varying number of grid cells and random arrangements of X_{CO_2} the viable number of grid cells was found to be between $n = 4$ up to 49 without considerable loss of capability to recover the true X_{CO_2} . Various inversions with random distribution of random X_{CO_2} (drawn from a normal distribution with mean and standard deviations from the data presented in Fig. 5) were carried out that all yielded good recovery of X_{CO_2} . For the real data, however, already for $n > 16$ the inversion yielded unreasonable high or low X_{CO_2} , that is, oscillating X_{CO_2} . The difference between the synthetic and the real data vector a is that the former exhibits a higher variability of Y_{CO_2} . This is illustrated in Fig. 7a, which shows the components of a for one of the synthetic model realizations and the real data. The real data shows high frequency components. One issue is the model discretization. In reality the scanned area was far from consisting of 16 grids with homogeneous X_{CO_2} only, but instead contained many spots, which leads to that spiky appearance of the real data vector. Further on, the more the “frozen” plume assumption holds the more

should the “humps” in Figure 7a resemble each other, since the x-axis on Figs. 7a and 7b scales with the time of acquisition. For the synthetic case, there are 5 somewhat similar, but distorted humps (Fig. 7b), due to the different viewing angle of each scan and differences in angle spans. It is, however, partially the case also for the real data vector (Fig. 7a), more so for the first 4 scans, less so for the last one. The spikes, i.e., the high frequency components, however, differ a lot, suggesting short lived fluctuations on a small spatial scale that do not reappear between subsequent scans. This high frequency “noise” is due to the fact that actual fluctuations of the X_{CO_2} occurred during the measurement. They happen on a faster time scale than the measurements of the 5 profiles (which took 142 minutes), violating our “frozen” plume assumptions, at least for small patches of CO_2 . This leads to inconsistencies between the system of linear equations (there is no solution that satisfies all equations simultaneously) and problems to fit the spiky data. Adding these high frequency components to the synthetic data by perturbing them by a random percentage using random perturbations and performing inversions gave an outcome very similar to the real data inversion. The inversion struggled to recover the true model X_{CO_2} (Fig. 7c), yielding oscillations. To improve the real data inversion result, synthetic inversions were performed after smoothing the perturbed synthetic data vector a (Fig. 7b). Low-pass filtering the data, however, removes peaks and therefore falsifies the data, which the iteration then tries to fit, yielding wrong X_{CO_2} . Smoothing had therefore to be applied with care. As a result, moderately smoothing the data using a running average with window size 14 yielded reasonable recovery of the true model (Fig. 7d). However, performing synthetic tests with a more than hundreds of random arrangements of the grid cells occasionally led to oscillations in the model, meaning that the true X_{CO_2} were over and undershot again. It is important to note that this occurred for grid cells at the model edges. This is the area where ray coverage is the poorest. It appeared that by increasing n this issue worsened. The inverse problem is then still overdetermined in the sense of ray coverage (for instance, for $n=64$ on average there are still 10 rays per grid cell). However, this is not the case for the edge grid cells, as some grid cells are not traversed by some rays, which is aggravated with increasing n , making the system mixed determined. This leads to the existence of non-unique solutions making the problem ill-posed (Zhang et al., 2016). Another contribution to the inconsistency of the system of linear equations is given by rays that are not traversing the edge grid cells due to the topography of the hard target (slope). These two issues are illustrated in Fig. 7e.

A more successful measure was to omit a part of the rays, which is effectively smoothing the data vector without falsifying it, so that inconsistencies in Eq. (7) are reduced. Best results were obtained by selecting only every third ray and the corresponding Y_{CO_2} as input to the inversion.

As for the synthetic tests, a constant X_{CO_2} , the mean of the raw data (Fig. 5), was used as a starting model for inverting the real data. As a consequence of the discussion above the maximum feasible number of grid cells was $n = 16$ for a robust inversion. The resulting grid length was $\Delta x = 38$ m and $\Delta y = 33$ m. The inverted model is shown in Figure 8a. To increase spatial resolution the inverted model was interpolated onto a grid with grid spacing $\Delta x/8$ and $\Delta y/8$ using ordinary Kriging interpolation. The result is shown in Fig. 8b. The zones without ray coverage were excluded from the 2-D map. Overlaying the resulting 2-D map of CO_2 mixing ratios with the map of Solfatara reveals a zone of increased anomalous CO_2 degassing

activity along the southeastern edge of Solfatara, which is in reasonable agreement with in situ data from the LICOR CO₂ analyzer (Fig. 8c).

The resulting 2-D map of CO₂ mixing ratios was used to compute the CO₂ flux. The vertical component of the plume transport speed was estimated to be $1.1 \pm 0.2 \text{ m s}^{-1}$. The plume speed uncertainty was retrieved from the standard deviation of various plume speeds retrieved from different tracks carried out across the plume (Queißer et al., 2016). Equation 10 was employed to estimate the flux uncertainty. Since the synthetic test inversions behave very similar to the real data inversion, to obtain a meaningful model uncertainty of the real data inversion 1000 synthetic inversions with random true models, drawn from a normal distribution using mean and standard deviation of the data presented in Figure 5 were carried out. Computing the absolute difference between true and recovered X_{CO_2} at each model grid point yielded 16×1000 values with a mean of 373 ppm. This was adopted as a measure for the model standard deviation of the real data inversion in Eq. (10), assuming it being constant throughout the model. The model error gave the most dominant uncertainty, associated to relative errors of the inverted X_{CO_2} between 34% and 90%. A constant $\Delta X_{CO_2,pl} = \max(\Delta X_{CO_2,av})$, i.e. the maximum error of all five scans, was considered for the measurement error. Using Eq. (8) the resulting CO₂ flux was computed as $17.0 \pm 9.2 \text{ kg s}^{-1} (\pm 1 \text{ SD})$ or $1465 \pm 798 \text{ tons day}^{-1}$.

4 Discussion

Retrieving CO₂ path amounts using calibration based on mixing ratios as done here is not optimal as the mixing ratios depend on temperature, pressure and humidity of the air. It was a solution that was adopted for practical reasons. Compared with the precision of the instrument the resulting bias was, however, low and could be neglected. Typically, the air temperature varied between 11 to 15°C, relative humidity varied between 55% and 65%. The air pressure was steady around 974 hPa. In a simplified estimation, this corresponds to a bias of ~1.5% of the total column averaged mixing ratio, which would correspond to around 9 ppm, assuming typical measured path amounts and ranges. To put this into context, the error of the column averaged mixing ratio was typically ~110 ppm (Fig. 3) and is dominated by the instrument SNR. The associated increase in flux uncertainty would be less than 1%. In the future, however, a better retrieval scheme will be adopted. This is important as we strive to increase in the measurement precision of the CO₂DIAL to sense more subtle CO₂ emissions than at Solfatara and a bias related to uncertainty of the number density becomes relevant. Note that a bias of 20 ppm due to uncertainties in background mixing ratio would also entail a small decrease in measurement precision by ~4% and an increase in flux error by roughly 2%.

The retrieved 2-D map (Fig. 8c) indicates an elongated zone of intense anomalous degassing along the eastern edge of the Solfatara crater. Encouragingly, this is a persistent feature in different inversions performed with different number of beam paths and smoothing parameters of input data and underpins that it is real. Previous measurements sampling the Solfatara area with accumulation chambers yielded an increased anomalous CO₂ degassing activity in the corresponding area too

(Granieri et al., 2010; Tassi et al., 2013; Bagnato et al., 2014). The retrieved elongated zone of anomalous CO₂ degassing likely encompasses at least two major vents (Fig. 8c). The locations of the peaks in CO₂ mixing ratio in Fig. 8c fairly agree with the 1-D input data. For instance, the peak near the center of the crater corresponds to the peak near 26° in the first scan in Fig. 3a. The second scan (Fig. 3b) indicates a rather abrupt decrease in $X_{CO_2,av}$ at 28°, in line with the edge of the zone of elevated CO₂ mixing ratios at the crater center (left part of Fig. 8c). This central degassing feature is coherent with results of recent campaigns (Granieri et al., 2010; Tassi et al., 2013; Bagnato et al., 2014). The increase in $X_{CO_2,av}$ near 9° in Fig. 3d matches the position of the local peak in X_{CO_2} between in situ points 7 and 8 in Fig. 6c. Provided sufficient ray, which was the case for the zones away from the edges of the 2-D map, disagreement between the peaks in the 1-D data (Fig. 3) and those in the 2-D map (Fig. 6) are likely due to physical fluctuations in CO₂ concentration (“frozen” plume approximation), as evinced in the result section. During acquisition one could visually identify at least 5 small vents emitting water vapor and therefore most likely also CO₂. Though not recovered due to the limited spatial and temporal resolution of the inversion this advocates that there are in fact separate vents south of the main vents, near the edge of the Solfatara crater.

Retrieved X_{CO_2} peak near 1300 ppm (2 m above ground), in line with the in situ LICOR data, although not spatially matching them in places. This can be explained by the fact that the in situ values were acquired the day before so that local wind and thus dispersion patterns were different. Nevertheless, both the LICOR in situ data and the inversion result indicate high X_{CO_2} near the main vents and along the crater edge. Near the main vents highest CO₂ mixing ratios in the 2-D map are located ca. 17 m west of BN. In fact, the whole zone of high X_{CO_2} is shifted ~17 m northwest from where one would expect it. Since the predominant wind direction at the time of acquisition was around 300°, to first order one would expect the CO₂ to disperse rather towards southeast, along the crater edge. The main vent area was at the edge of the scanned area. Note that the relative inversion residual $\|a - Lc\|/\|a\|$ was 0.18, which means on average 18% of $\Delta X_{CO_2,pl}$ are unexplained by the model in Fig. 8a. Note that due to the non-uniqueness of the problem a lower misfit does not imply that the inverted model is closer to the “true” model. For instance, increasing grid number decreased the misfit, but yielded models with X_{CO_2} much larger or lower than the minimum in Fig. 4 indicating oscillation and hence unrealistic model. Although being close to the expected distribution, the mismatch is therefore likely due to a non-unique realization of the model. The latter is related to poor ray coverage for grid 16, which is partly corresponding to the zone containing the main vents, and the error resulting from the low model discretization (in reality X_{CO_2} was certainly not constant over 30 m). Note that the acquisition focused on the zone south of the main vents. Possibly, but less likely, CO₂ was advected slightly towards west due to dispersive mechanism related to local wind eddies decoupled from the main wind direction. These dispersive mechanisms take place in any case and make a distinction between CO₂ from the main vents and the surrounding diffuse degassing challenging. For that reason, in future acquisitions at that site the region of interest shall be scanned from instrument positions aligned along a half circle around the zone rather than using a “flat” scan geometry as chosen here.

For a comparison, CO₂ fluxes were computed directly from the 1-D profiles, that is, similar to Eq. (8) but using path amounts, ignoring any heterogeneity in the CO₂ distribution. Given the uncertainty, the average flux of all five scans (1055 ± 389 tons/day) is compatible with the result obtained from the 2-D map (1465 ± 798 tons day⁻¹).

Yet, both the CO₂ flux from the 2-D map and from the 1-D profiles are higher than fluxes previously estimated. Pedone et al. (2014) report a CO₂ flux of only ~300 tons/day in early 2013, however, it focused on the area around the Solfatara main vents, that is, 8000 m². In this study the area considered for flux computation was over 21000 m². Moreover, the average degassing rate at Solfatara has been increasing by ~9% each year over the past 10 years or so (Chiodini et al., 2010; d'Auria, 2015). The magnitude of the retrieved flux of this work equals the total CO₂ flux of DDS (diffuse degassing structure, which encompasses Solfatara crater, the Pisciarelli fumaroles and the area around Solfatara crater) reported by Granieri et al. (2003), however, 13 years prior to this study, when emission rates were 1.09¹³ (or 3) times lower. A very rough extrapolation of the 1465 tons day⁻¹ obtained here to the whole of Solfatara crater, that is, by assuming a constant flux per unit area (Queißer et al., 2016) would yield a flux between 2400 and 4700 tons day⁻¹. This makes 1465 tons day⁻¹ a coherent figure. Extrapolating the flux for the main vent area of 300 tons/day from 2013 would yield a flux of 390 tons/day in early 2016. Integrating CO₂ mixing ratios of the area around the main vents only (bounded to the south by in situ point 6, Fig. 6c) yields a flux of 364 ± 206 tons day⁻¹ of CO₂, in excellent agreement with the extrapolated flux. Finally, we note that to our knowledge all former studies except one (Pedone et al., 2014) inferred X_{CO_2} and hence CO₂ fluxes from a grid of point measurements. If the area associated with lower CO₂ concentration was larger than the area with very high CO₂ concentration, point sampling may have missed degassing activity in between the measurement points and so tended to yield lower flux values.

All five scans were performed one-sided, i.e. from a single half space, as often the case in geophysical tomography problems (e.g. Hobro et al., 2003). As evinced above, this was not ideal for any inversion technique as it makes the inverse problem mixed determined, leading to a non-unique solution, meaning that many models may explain the observed data equally well. However, for Solfatara there is an abundance of hard data available, which extremely facilitated the rejection of unlikely models. This case therefore enabled to demonstrate that one may obtain useful tomographic results from one-sided scanning of a degassing feature. A coarse grid spacing was necessary to exclude non-unique solutions, which arose at grid numbers $n > 16$. As a consequence the inverted model is missing small-scale features. Nevertheless, given the fair agreement with the hard data, the inverted 2-D model (Fig. 6c) is quantitatively sound and outlines the geometry of the diffuse degassing probed at Solfatara. Future measurements of this type at Solfatara are envisaged, including a more systematic study, using a wider variety of viewing angles, which will allow a better assessment as to which extent this method is useful for one-sided tomography of highly non-isotropic CO₂ plumes in nature. We expect an enlarged angle diversity to increase the maximum number of grids usable for stable inversion, boosting 2-D resolution.

5 Conclusions

As magmatic CO₂ degassing rates are tracers for the dynamics and chemistry of the magma plumbing system beneath Campi Flegrei and at volcanic areas in general, a comprehensive quantification of magmatic CO₂ degassing strength is of interest for volcanology and of vital importance for civil protection.

5 Scanning hard target DIAL measurements have been performed at Solfatara crater (Campi Flegrei, Italy), which allowed an inclusive measurement of CO₂ amounts in the form of 1-D profiles of CO₂ path amounts. From the 1-D profiles a 2-D map of CO₂ mixing ratios X_{CO_2} has been reconstructed outlining the main CO₂ distribution. The one-sided acquisition geometry of the 1-D profiles, which were input to the inversion, was not ideal for a tomographic reconstruction and for $n > 16$ led to erroneous mixing ratios near the model edge, strongly limiting spatial resolution of the inverted model. Furthermore, 10 assumptions about the emission dynamics had to be made (“frozen” plume). Yet, the resulting map of X_{CO_2} was in satisfactory agreement with independent measurements of CO₂ mixing ratio. Therefore, the 2-D map was deemed to be useful to retrieve the CO₂ flux. The fluxes retrieved using that map is compatible with previous results. The 1-D profiles have been acquired from a single half space (one-sided), which indicates this tomography method to be potentially beneficial for scanning strongly non-isotropic CO₂ distributions, such as diffuse emissions, that can be viewed from limited angles only, sites difficult to access 15 (e.g. volcanic craters), or airborne acquisitions. To validate the latter and to fully assess the potential of this method future acquisitions are planned that involve different scanning geometries, possibly allowing for an enhanced resolution of the 2-D map and thus more accurate gas flux estimation.

Acknowledgments

20 The research leading to these results has received funding from the European Research Council under the European Union’s Seventh Framework Programme (FP/2007-2013)/ERC Grant Agreement n. 279802. Our gratitude goes to Rosario Avino and Antonio Carandente (INGV Osservatorio Vesuviano), who sampled the in situ CO₂ mixing ratios. We thank Graham Allen (NASA Goddard) and Luca Fiorani (ENEA) for sharing extremely valuable experiences in LIDAR development with us.

25

References

Aiuppa, A., Burton, M., Allard, P., Caltabiano, T., Giudice, G., Gurrieri, S., Liuzzo, M., Salerno, G.: First observational evidence for the CO₂-driven origin of Stromboli’s major explosions, *Solid Earth*, 2, 135-142, 2011.

- Aiuppa, A., Tamburello, G., Di Napoli, R., Cardellini, C., Chiodini, G., Giudice, G., Grassa, F., and Pedone, M.: First observations of the fumarolic gas output from a restless caldera: Implications for the current period of unrest (2005–2013) at Campi Flegrei, *Geochem. Geophys. Geosyst.*, 14, 4153-4169, 2013.
- 5 Aiuppa, A., Fiorani, L., Santoro, S., Parracino, S., Nuvoli, M., Chiodini, G., Minopoli, C., and Tamburello, G.: New ground-based lidar enables volcanic CO₂ flux measurements, *Sci. Rep.*, 5, 13614; doi: 10.1038/srep13614, 2015.
- Amediek, A., Fix, A., Wirth, M., and Ehret, G.: Development of an OPO system at 1.57 μm for integrated path DIAL measurement of atmospheric carbon dioxide, *Appl. Phys. B*, 92, 295-302, 2008.
- 10 d'Auria, L.: Update sullo stato dei Campi Flegrei, INGV, Sezione di Napoli, Report, available at ftp://ftp.ingv.it/pro/web_ingv/Convegno_Struttura%20_Vulcani/presentazioni/15_D'auria_CampiFlegrei/dauria_cf.pdf, accessed in May 2016, 2015.
- 15 Bagnato, E., Barra, M., Cardellini, C., Chiodini, G., Parello, F., and Sprovieri, M.: First combined flux chamber survey of mercury and CO₂ emissions from soil diffuse degassing at Solfatara of Pozzuoli crater, Campi Flegrei (Italy): Mapping and quantification of gas release, *J. Volcanol. Geotherm. Res.*, 289, 26-40 2014.
- Baubron, J. C., Allard, P., Sabroux, J. C., Tedesco, D., Toutain, J.P.: Soil gas emanations as precursory indicators of
20 volcanic eruptions, *J. Geol. Soc. London* 148, 571-576, 1991.
- Burton, M. R., Sawyer, G. M., and Granieri, D.: Deep carbon emissions from Volcanoes, *Rev. Mineral. Geochem.*, 75, 323-354, 2013.
- 25 Carapezza, M. L., Inguaggiato, S., Brusca, L., and Longo, M.: Geochemical precursors of the activity of an open-conduit volcano: The Stromboli 2002-2003 eruptive events, *Geophys. Res. Lett.*, 31, L07620, 2004.
- Chiodini, G., Baldini, A., Barberi, F., Carapezza, M. L., Cardellini, C., Frondini, F., Granieri, D., and Ranaldi, M.: Carbon dioxide degassing at Latera caldera (Italy): Evidence of geothermal reservoir and evaluation of its potential energy, *J. Geophys. Res.*, 112, B12204, 2007.
- 30 Chiodini, G., Caliro, S., Cardellini, C., Granieri, D., Avino, R., Baldini, A., Donnini, M., and C. Minopoli.: Long-term variations of the Campi Flegrei, Italy, volcanic system as revealed by the monitoring of hydrothermal activity, *J. Geophys. Res.*, 115, B03205, doi:10.1029/2008JB006258, 2010.

Chiodini, G., Caliro S., Aiuppa, A., Avino, R., Granieri, D., Moretti, R., and Parello, F.: First $^{13}\text{C}/^{12}\text{C}$ isotopic characterisation of volcanic plume CO_2 , *Bull. Volcanol.*, 73, 5:531-542, doi: 10.1007/s00445-010-0423-2, 2011.

5 Chiodini, G., Pappalardo, L., Aiuppa, A., and Caliro, S.: The geological CO_2 degassing history of a long-lived caldera, *Geology*, 43, 767-770, 2015.

Diaz, J. A., Pieri, D., Arkin, C. R., Gore, E., Griffin, T. P., Fladeland, M., Bland, G., Soto, C., Madrigal, Y., Castillo, D., Rojas, E., and Achi, S.: Utilization of in situ airborne MS-based instrumentation for the study of gaseous emissions at active
10 volcanoes, *Int. J. Mass Spectrom.*, 295, 105-112, 2010.

Dobler, J. T., Harrison, F. W., Browell, E. V., Lin, B., McGregor, D., Kooi, S., Choi, Y., and Ismail, S.: Atmospheric CO_2 column measurements with an airborne intensity-modulated continuous-wave 1.57-micron fiber laser lidar, *Appl. Optics*, 52, 2874-2894, 2013.

15 Frezzotti, M.-L. and Touret, J. L. R.: CO_2 , carbonate-rich melts, and brines in the mantle, *Geosci. Front.*, 5, 697-710, 2014.

Galle, B., Johansson, M., Rivera, C., Zhang, Y., Kihlman, M., Kern, C., Lehmann, T., Platt, U., Arellano, and S., Hidalgo, S.: Network for Observation of Volcanic and Atmospheric Change (NOVAC)-A global network for volcanic gas monitoring:
20 Network layout and instrument description, *J. Geophys. Res.*, 115, D05304, doi:10.1029/2009JD011823, 2010.

Gerlach, T. M., Delgado, H., McGee, K. A., Doukas, M. P., Venegas, J. J., Cárdenas, L.: Application of the LI-COR CO_2 analyzer to volcanic plumes: A case study, volcán Popocatepetl, Mexico, June 7 and 10, 1995, *J. Geophys. Res.*, 102, 8005-8019, 1997.

25 Granieri, D., Chiodini, G., Marzocchi, W., and Avino, R.: Continuous monitoring of CO_2 soil diffuse degassing at Phlegraean Fields (Italy): influence of environmental and volcanic parameters, *Earth Planet. Sci. Lett.*, 212, 167-179, 2003.

Granieri, D., Avino, R., Chiodini, G.: Carbon dioxide diffuse emission from the soil: ten years of observations at Vesuvio
30 and Campi Flegrei (Pozzuoli), and linkages with volcanic activity, *Bull. Volcanol.*, 72, 103-118, doi:10.1007/s00445-009-0304-8, 2010.

Granieri, D., Carapezza, M. L., Barberi, F., Ranaldi, M., Ricci, T., and L. Tarchini.: Atmospheric dispersion of natural carbon dioxide emissions on Vulcano Island, Italy, *J. Geophys. Res. Solid Earth*, 119, doi:10.1002/2013JB010688, 2014.

- Hards, V. L.: Volcanic contributions to the global carbon cycle, British Geological Survey Occasional Report No. 10, 26pp., 2005.
- 5 Hobro, J. W. D., Singh, S. C., and Minshull, T. A.: Three-dimensional tomographic inversion of combined reflection and refraction seismic travelttime data, *Geophys. J. Int.*, 152, 79-93, 2003.
- Johansson, M., Galle, B., Rivera, B., and Zhang, Y.: Tomographic reconstruction of gas plumes using scanning DOAS, *Bull. Volcanol.*, 71, 1169-1178, 2009.
- 10 Kameyama, S., Imaki, M., Hirano, Y., Ueno, S., Kawakami, S., Sakaizawa, D., and Nakajima, M.: Development of 1.6 μm continuous-wave modulation hard-target differential absorption lidar system for CO_2 sensing, *Opt. Lett.*, 34, 1513-1515, 2009.
- Kazahaya, R., Mori, T., Kazahaya, K., and Hirabayashi, J.: Computed tomography reconstruction of SO_2 concentration
15 distribution in the volcanic plume of Miyakejima, Japan, by airborne traverse technique using three UV spectrometers, *Geophys. Res. Lett.*, 35, L13816, 2008.
- Koch, G. J, Barnes, B. W., Petros, M., Beyon, J. Y., Amzajerjian, F., Yu, J., Davis, R. E, Ismail, S., Vay, S., Kavaya, M. J, and Singh, U. N.: Coherent differential absorption lidar measurements of CO_2 , *Appl. Optics*, 43, 5092-5099, 2004.
- 20 La Spina, G., Burton, M., and de Vitturi, M.: Temperature evolution during magma ascent in basaltic effusive eruptions: A numerical application to Stromboli volcano, *Earth Planet. Sci. Lett.*, 426, 89-100, 2015.
- Lee, H, Muirhead, J. D, Fischer, T. P, Ebinger, C. J, Kattenhorn, S. A, Sharp, Z. D., and Kianji, G.: Massive and prolonged
25 deep carbon emissions associated with continental rifting, *Nature Geosci.*, 9, 145-149, 2016.
- Lewicki, J. L., Bergfeld, D., Cardellini, C., Chiodini, G., Granieri, D., Varley, N., Werner, C.: Comparative soil CO_2 flux measurements and geostatistical estimation methods on Masaya volcano, Nicaragua, *Bull. Volcanol.*, 68, 76-90, 2005.
- 30 McGee, K. A., Doukas, M. P., McGimsey, R. G., Neal, C. A., and Wessels, R. L.: Atmospheric contribution of gas emissions from Augustine volcano, Alaska during the 2006 eruption, *Geophys. Res. Lett.*, 35, L03306, doi:10.1029/2007GL032301, 2008.

- MacKerrow, E. P, Schmitt, M. J., and Thompson, D. C.: Effect of speckle on lidar pulse-pair ratio statistics, *Appl. Optics*, 36, 8650-8669, 1997.
- Menzies, R. T. and Chahine, M. T.: Remote Atmospheric Sensing with an Airborne Laser Absorption Spectrometer, *Appl. Opt.*, 13, 2840-2849, 1974.
- Oliver, M. A.: Kriging: a method of estimation for environmental and rare disease data, *Geo. Soc., London, Special Publications*, 113, 245-254, doi: 10.1144/GSL.SP.1996.113.01.21, 1996.
- 10 Pedone, M., Aiuppa, A., Giudice, G., Grassa, F., Cardellini, C., Chiodini, G., and Valenza, M.: Volcanic CO₂ flux measurement at Campi Flegrei by Tunable Diode Laser absorption Spectroscopy, *Bull. Volc.*, 76, doi: 10.1007/s00445-014-0812-z, 2014.
- Platt, U., Lübke, P., Kuhn, J., Bobrowski, N., Prata, F., Burton, M., Kern, C.: Quantitative imaging of volcanic plumes -Results, needs, and future trends, *J. Volcanol. Geotherm. Res.*, 300, 7-21, 2015.
- 15 Petrazzuoli, S. M., Troise, C., Pingue, F., and DeNatale, G.: The mechanisms of Campi Flegrei unrests as related to plastic behaviour of the caldera borders, *Ann. Geofis.*, 42, 529-544, 1999.
- Queißer, M., Burton, M., and Fiorani, L.: Differential absorption lidar for volcanic CO₂ sensing tested in an unstable atmosphere, *Opt. Express*, 23, 6634-6644, 2015a.
- 20 Queißer, M., Granieri, D., Burton, M., La Spina, A., Salerno, G., Avino, R., and Fiorani, L.: Intercomparing CO₂ amounts from dispersion modeling, 1.6 µm differential absorption lidar and open path FTIR at a natural CO₂ release at Caldara di Manziana, Italy, *Atmos. Meas. Tech. Discuss.*, 8, 4325-4345, 2015b.
- 25 **Queißer, M., Granieri, D., Burton, M.: A new frontier in CO₂ flux measurements using a highly portable DIAL laser system, *Sci. Rep.*, 6, 33834, 2016.**
- Rothman, L. S., Gordon, I. E., Babikov, Y., Barbe, A., Benner, D. C., Bernath, P. F., Birk, M., Bizzocchi, L., Boudon, V., Brown, L. R., Campargue, A., Chanc, K., Coudert, L., Devi, V. M., Drouin, B. J., Fayt, A., Flaud, J.-M., Gamache, R. R., Harrison, J., Hartmann, J.-M., Hill, C., Hodges, J. T., Jacquemart, D., Jolly, A., Lamouroux, J., LeRoy, R. J., Li, G., Long, D., Mackie, C. J., Massie, S. T., Mikhailenko, S., Müller, H. S. P., Naumenko, O. V., Nikitin, A. V., Orphal, J., Perevalov, V., Perrin, A., Polovtseva, E. R., Richard, C., Smith, M. A. H., Starikova, E., Sung, K., Tashkun, S., Tennyson, J., Toon, G. C.,
- 30

Tyuterev, V. G., Auwera, J. V., and Wagner, G.: The HITRAN 2012 Molecular Spectroscopic Database, *J. Quant. Spectrosc. Ra.*, 130, 4-50, 2013.

5 Sakaizawa, D., Nagasawa, C., Nagai, T., Abo, M., Shibata, Y., Nakazato, M., and Sakai, T.: Development of a 1.6 μm differential absorption lidar with a quasi-phase-matching optical parametric oscillator and photon-counting detector for the vertical CO_2 profile, *Appl. Optics*, 48, 748-757, 2009.

10 Sakaizawa, D., Kawakami, S., Nakajima, M., Tanaka, T., Morino, I., and Uchino, O.: An airborne amplitude modulated 1.57 μm differential laser absorption spectrometer: simultaneous measurement of partial column-averaged dry air mixing ratio of CO_2 and target range, *Atmos. Meas. Tech.*, 6, 387-396, 2013.

Scarpati, C., Cole, P., and Perrotta, A.: The Neapolitan Yellow Tuff- A large volume multiphase eruption from Campi Flegrei, Southern Italy, *Bull. Volcanol.*, 55, 343-356, 1993.

15 Tassi, F., Nisi, B., Cardellini, C., Capecchiacci, F., Donnini, M., Vaselli, O., Avino, R., and Chiodini, G.: Diffuse soil emission of hydrothermal gases (CO_2 , CH_4 and C_6H_6) at the Solfatara crater (Phlegraean Fields, southern Italy), *Appl. Geochem.*, 35, 142-153, 2013.

20 Weibring, P., Edner, H., Svanberg, S., Cecchi, G., Pantani, L., Ferrara, R., Caltabiano, T.: Monitoring of volcanic sulphur dioxide emissions using differential absorption lidar (DIAL), differential optical absorption spectroscopy (DOAS), and correlation spectroscopy (COSPEC), *Appl. Phys. B*, 67, 419-426, 1998.

Wright, T. E., Burton, M. R., Pyle, D. M., and Caltabiano, T.: Scanning tomography of SO_2 distribution in a volcanic gas plume, *Geophys. Res. Lett.*, 35, L17811, doi: 10.1029/2008GL034640, 2008.

25

Zhang, Y., Gulliksson, M., Hernandez Bennetts, and V. M., Schaffer, E.: Reconstructing gas distribution maps via an adaptive sparse regularization algorithm, *Inverse Problems in Science and Engineering*, 24, 1186-1204, 2016.

30

5

10

Tables

15

k	$x_{1,k}$ (m)	$y_{1,k}$ (m)	Y_{CO_2} (ppm.m)	$X_{CO_2,av}$ (ppm)
1	0	0	65273.46	679.93
2	0.947	-0.155	65273.46	679.93
3	1.894	-0.310	65273.46	679.93
4	2.842	-0.465	65273.46	679.93
5	3.789	-0.620	65273.46	679.93

20

⋮

97	90.950	-14.880	65273.46	679.93
98	91.898	-15.035	65273.46	679.93
99	92.845	-15.190	65273.46	679.93
100	93.793	-15.345	65273.46	679.93

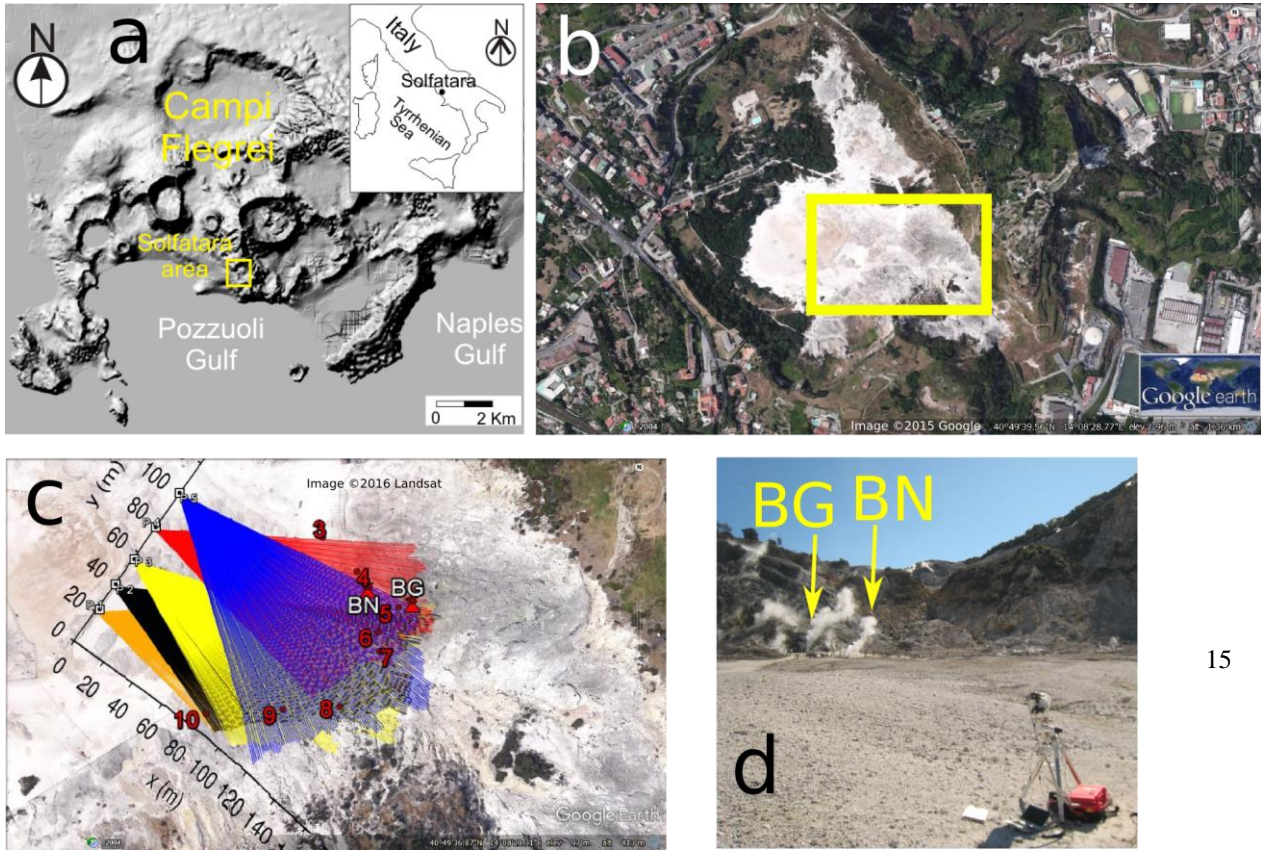
25

Table 1. Inversion data input file showing (x,y) coordinates with associated measured Y_{CO_2} and $X_{CO_2,av} = Y_{CO_2}/R_j$ of the first ray ($j = 1$) and $x_{j=1,k}$, $y_{j=1,k}$ for the first 5 and last 4 path length increments. $N = 100$.

30

Figures

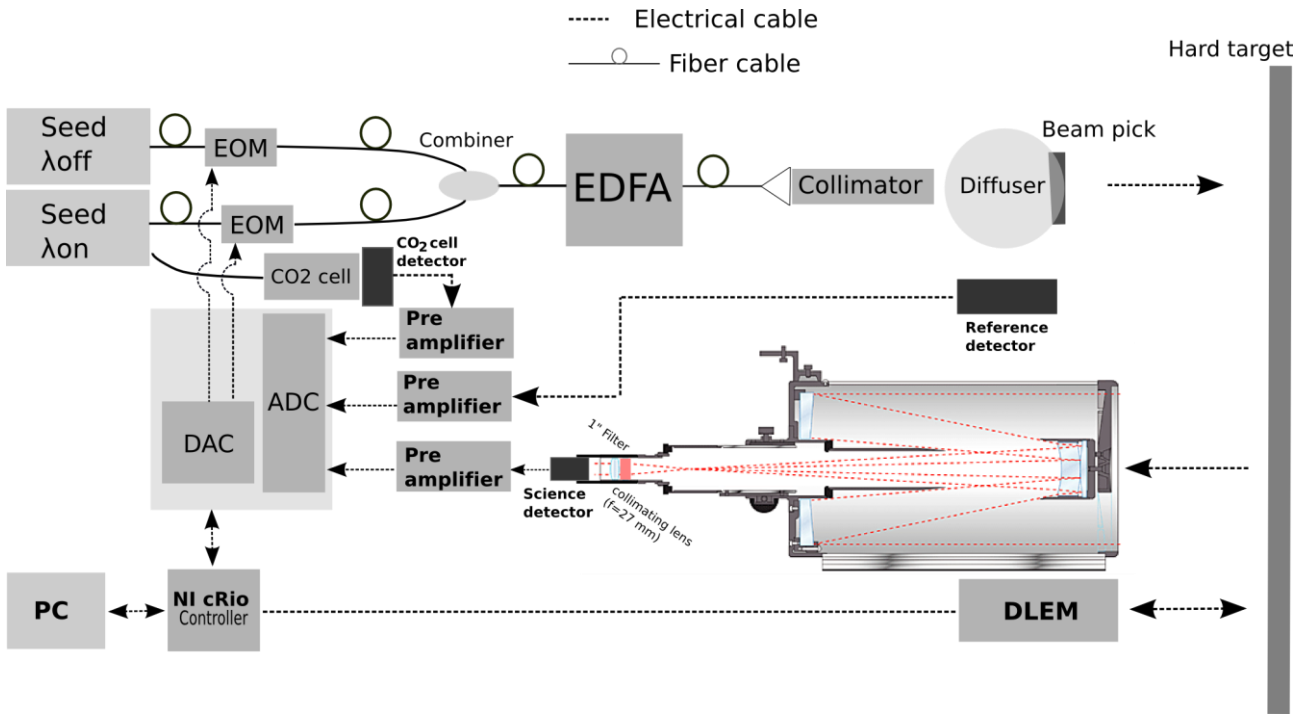
5



15

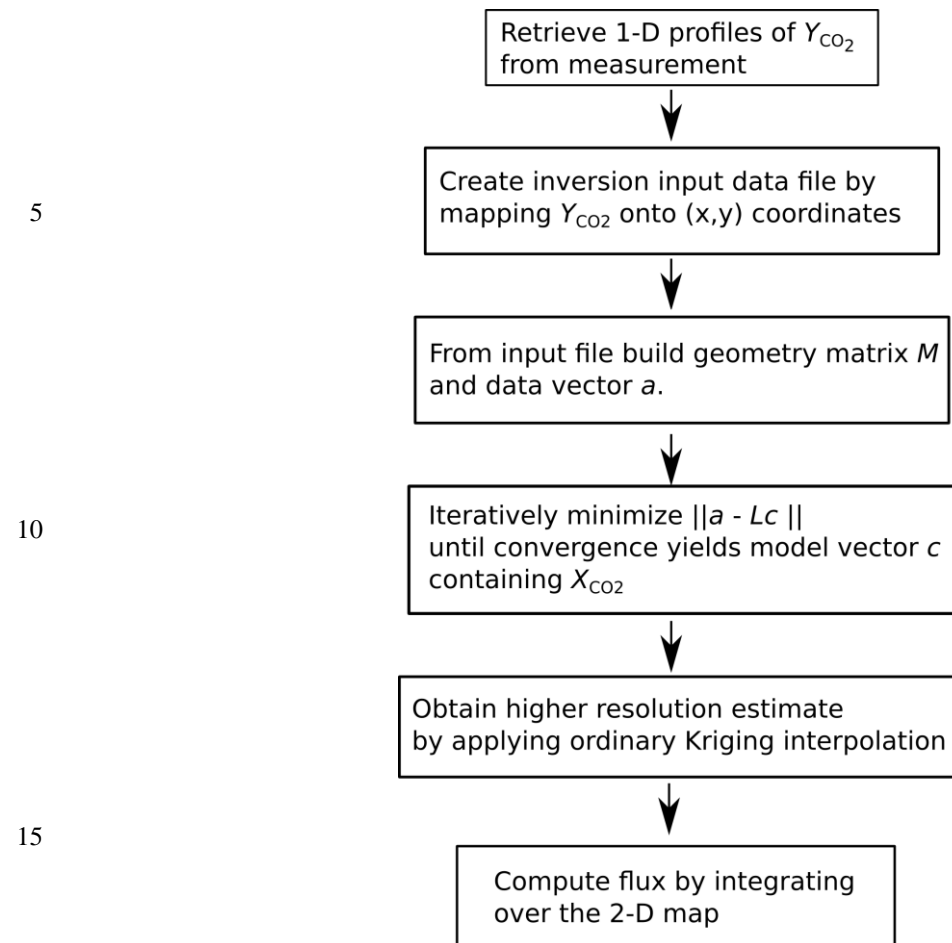
20 **Figure 1: Geography and measurement geometry.** (a) Location of the Solfatara crater as part of the volcanic area of Campi Flegrei, near Naples (Italy). (b) Nadir photo of Solfatara crater. The rectangle contains the region of interest. (c) Zoom of area outlined by the rectangle depicting the five instrument positions P1 to P5 with the following UTM-coordinates: P1: (427476, 4519921), P2: (427485, 4519935), P3: (427495, 4519949), P4: (427507, 4519967), P5: (427520, 4519986). Also shown are the respective range vectors (rays) for all five scans and the numbered locations of the LICOR measurements. (d) Photo taken during the scan at P5 looking towards east. The largest clouds of condensed water aerosol appeared near the main vents (Bocca Nuova, BN and Bocca Grande, BG) on the left. The CO₂DIAL, visible in the lower right corner, comprised of the tripod carrying the telescope (with transmitter unit) and the main unit (red box).

25

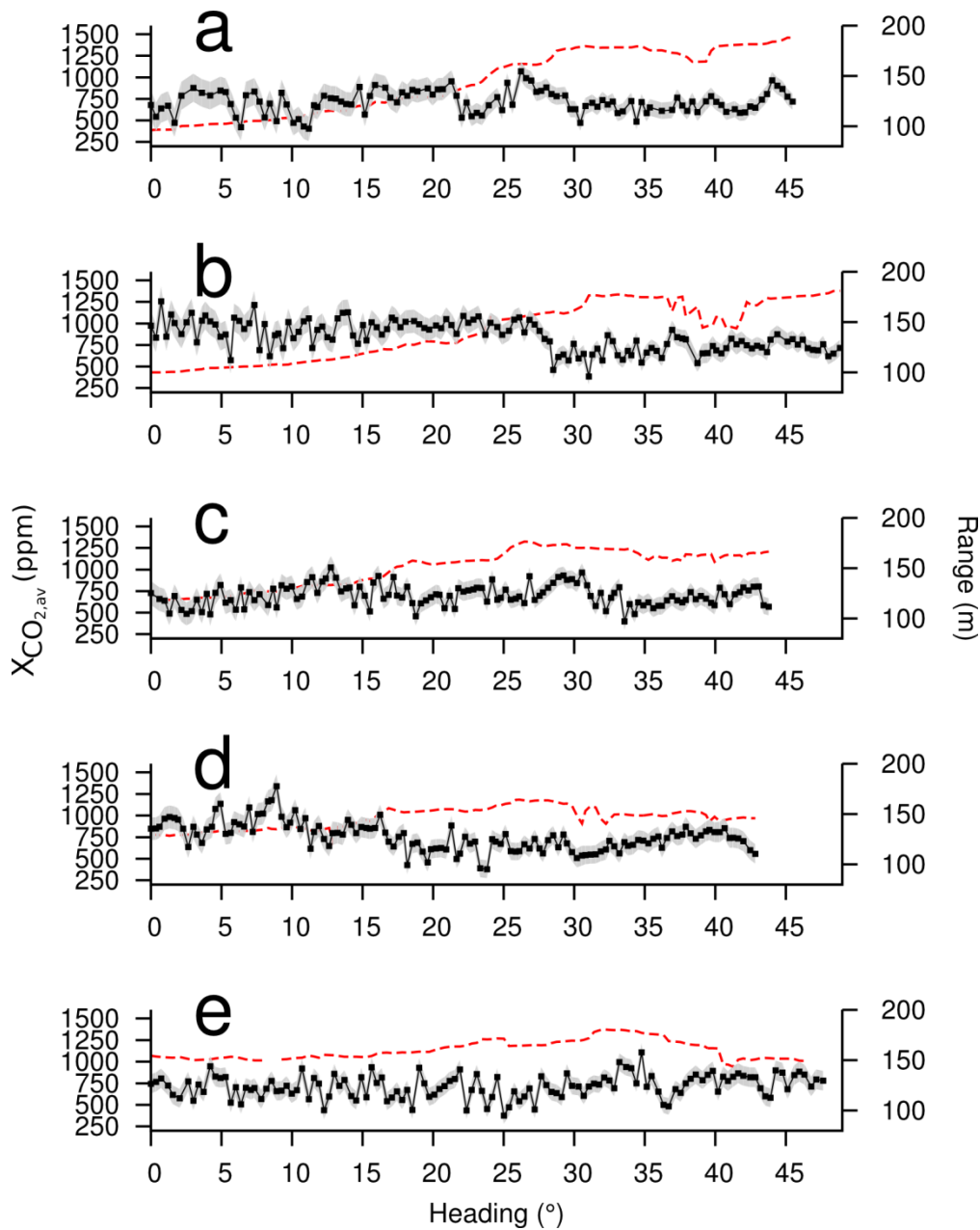


5 Figure 2: Scheme of the CO₂ DIAL as used for this experiment. EOM: Electro-optical modulator, DLEM: range finder module, EDFA: Erbium doped fiber amplifier. **The beam pick is a glass wedge and reflects part of the transmitted light back into an integrating sphere (depicted as diffuser).** ADC: analog-to-digital converter, DAC: digital-to-analog converter. The CO₂ cell is used to calibrate the seed laser wavelengths. To minimize hard target and turbulence related speckle noise the collimator used had a relatively high divergence of 1.7 mrad while the telescope field of view was 1.5 mrad. For mechanical reasons the optical band pass filter was mounted before the collimating lens. The change in transmission spectrum can be neglected.

10



20 **Figure 3: Scheme summarizing the main data processing steps involved in this paper.**



5 **Figure 4:** 1-D profiles of $X_{CO_2,av}$, the total (not background corrected) CO_2 mixing ratios, derived by dividing the path amounts Y_{CO_2} (ppm.m) per angle by the associated range. Each value therefore represents a column-averaged mixing ratio. Each point corresponds to 784 ms integration time. For each profile and heading ranges are indicated by the red dashed line. (a) Profile acquired between 9:35:36 and 9:41:54. (b) Profile acquired between 10:04:08 and 10:10:54. (c) Profile acquired between 10:31:24 and 10:37:28. (d) Profile acquired between 11:01:46 and 11:07:46. (e) Profile acquired between 11:50:39 and 11:57:15. The grey envelope depicts precision (1 SD, Eq. 3).

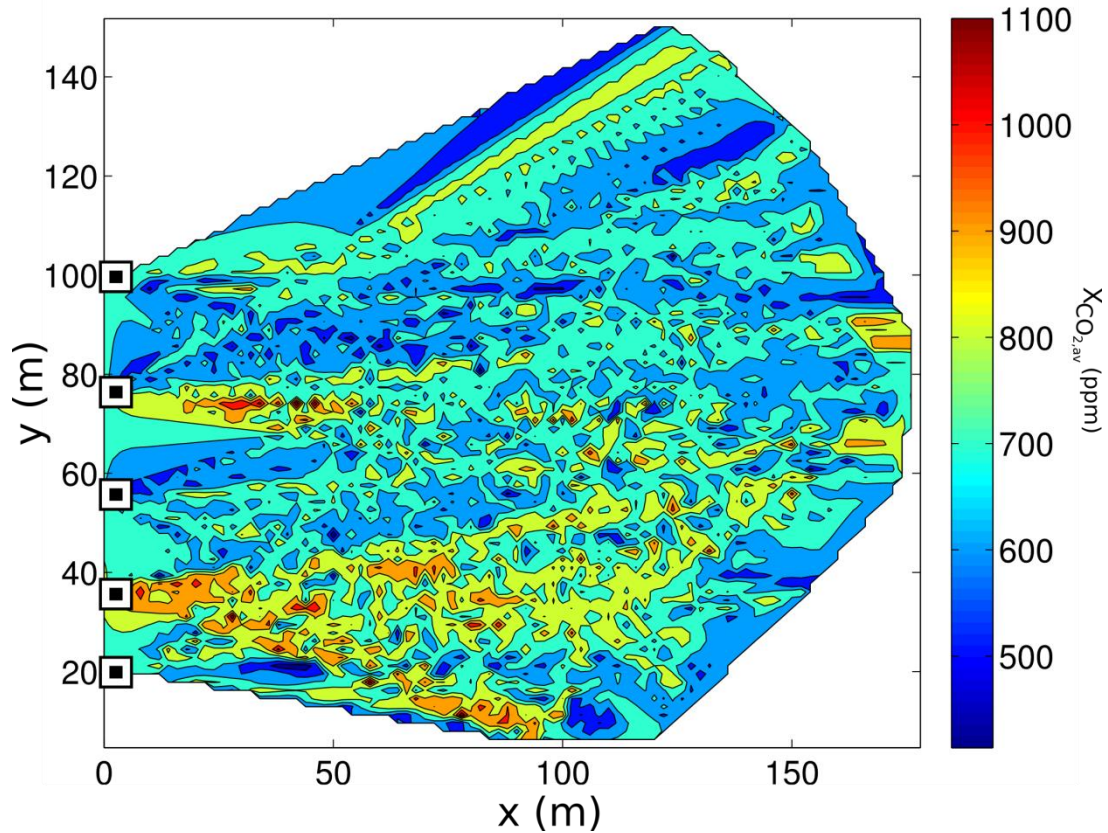
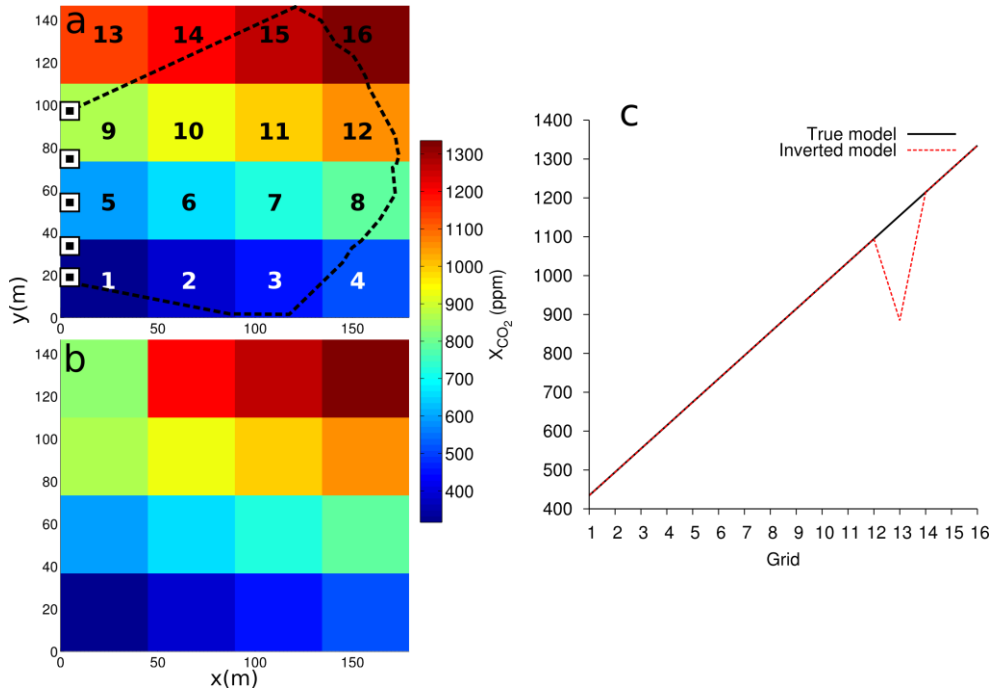


Figure 5: Contour plot of Y_{CO_2} after mapping them onto (x,y) coordinates (which is the input to the inversion), divided by the range for all 627 beam paths (same as shown in Table 1 for first ray), which yields column averaged mixing ratios $X_{CO_2,av}$. Also shown are the instrument positions (squares on y-axis) starting with P1 at $y = 20$ m. For display purposes the data has been regridded on a regular grid of 90×90 points using natural interpolation. One would expect high anomalous CO_2 mixing ratios near the main vents (BN, BG near $x = 120$ m, $y = 140$ m) and the southern part of the area. Low anomalous CO_2 mixing ratios are to be expected in the northwestern part. Note that due to the abundance of data some data points were masking each other. They were thus averaged, leading to a maximum mixing ratio lower than actually observed (e.g. in Fig. 4b).

20

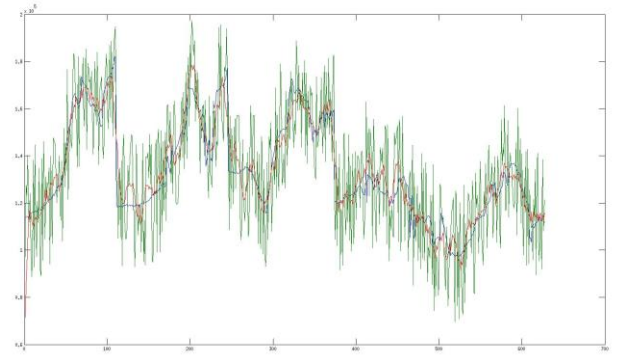
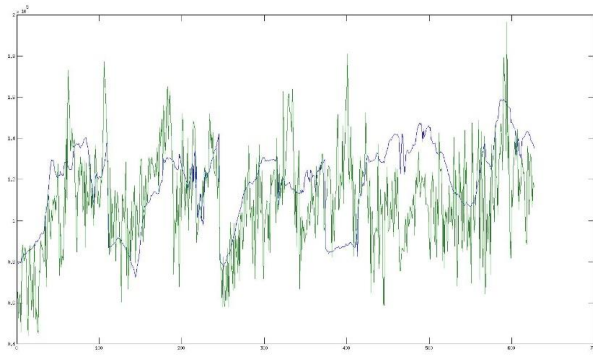
25



5

Figure 6: Synthetic inversion result with $n = 16$ grid cells. (a) True model used to generate synthetic column averaged Y_{CO_2} . Each grid cell is identified by a grid number. The dotted line outlines the ray coverage. The instrument positions are indicated. (b) Inverted model. (c) True and inverted X_{CO_2} versus grid cell. The inverted X_{CO_2} for grid 13 is off since the ray coverage associated with that area was poor.

10



5
10
15
20
25

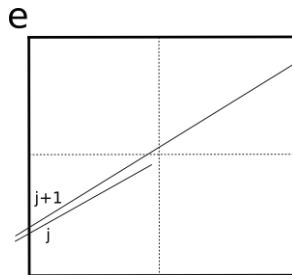
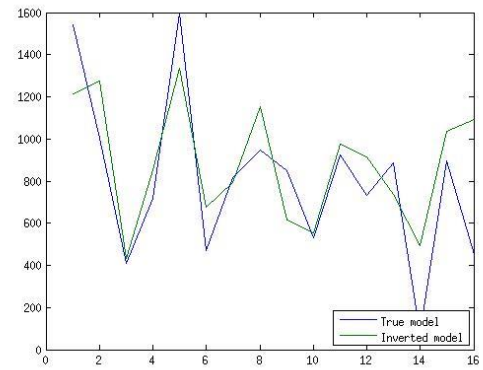
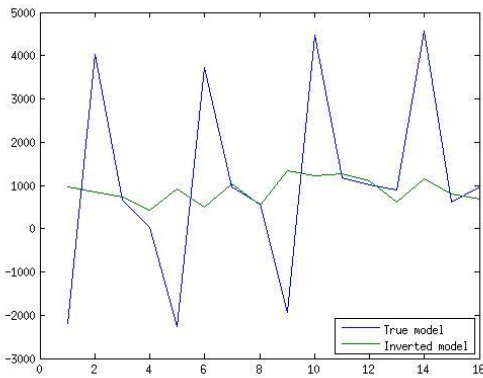
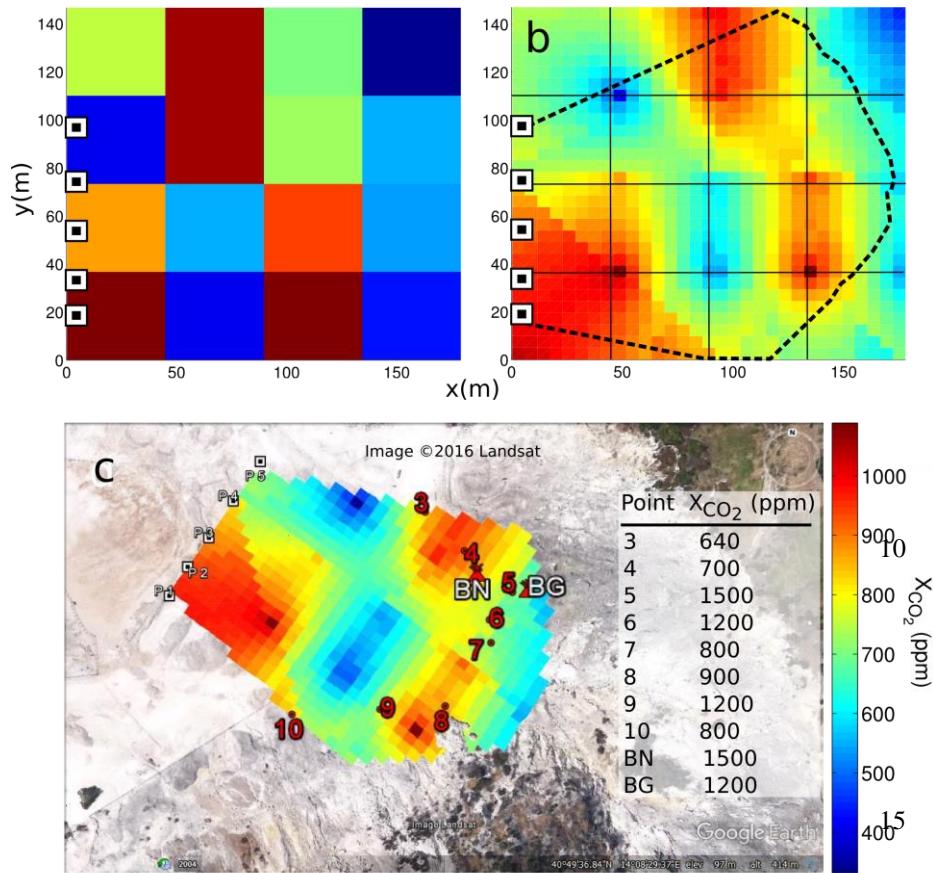


Figure 7: Synthetic inversion tests with perturbed data. (a) Data vector a (Eq. 7) showing the real data (green) and synthetic data (black, used for inversion result in Fig. 6b) versus ray number. (b) Synthetic data vector (blue), perturbed synthetic data vector (green) and smoothed perturbed synthetic data vector (red). (c) Inversion result using the perturbed synthetic data. (d) Inversion result using the smoothed perturbed synthetic data. (e) Scheme of a single grid cell at the model edge facing the instrument position with two subsequent rays. The length of ray j within this grid cell is smaller due to the topography. This leads to an under estimation of the path amount Y_{CO_2} with respect to ray $j+1$ and thus inconsistencies of Eq. (7). If the number of grid cells of the model is increase, for instance, such that the grid spacing is halved (dotted lines), this leads to grid cells without ray coverage and hence erroneous model values.

(Final figure will follow)



20 **Figure 8: Retrieved 2-D model of X_{CO_2} . (a) Inverted model of X_{CO_2} . (b) Inverted X_{CO_2} in after ordinary Kriging interpolation (interpolated grid size is 3.75 by 4.38 m). The ray coverage is depicted by the dotted line, while the straight lines outline the grid. (c) X_{CO_2} superposed onto nadir photo of Solfatara for those grid cells covered by the rays. To project the inverted model onto the map the function “overlay image” of Google Earth software has been used using altitude 0 relative to instrument altitude above ground. Also shown are the X_{CO_2} from in situ measurements (measurement points 3 to 10) using the LICOR CO_2 analyzer. Note that the in situ values had been acquired a day before the scans and thus serve as an approximate reference only. Moreover, measured column integrated mixing ratios were below 1500 ppm, so there are X_{CO_2} of 1500 ppm expected in the inversion result. The area in grids 4 and 16 bounded by the dotted line (arrow) are not excluded from the final 2-D map since, due to the weighting with neighbored values during Kriging interpolation, they carry valuable information.**

25